

Towards a full w CDM map-based analysis for weak lensing surveys

D. Zürcher,^{a,1} J. Fluri,^a V. Ajani,^a S. Fischbacher,^a A. Refregier,^a T. Kacprzak^{a,b}

^aInstitute for Particle Physics and Astrophysics, Department of Physics, ETH Zürich, Wolfgang Pauli Strasse 27, 8093 Zürich, Switzerland

^bSwiss Data Science Center, Paul Scherrer Institute, 5232 Villigen PSI, Switzerland

E-mail: dominikz@phys.ethz.ch

Abstract. The next generation of large scale weak lensing surveys will measure the matter distribution of the local Universe with unprecedented precision, allowing the resolution of non-Gaussian features of the convergence field. This encourages the use of higher-order mass-map statistics for cosmological parameter inference. However, the increased quality and quantity of the data poses new challenges for such map-based analyses. We extend the forward-modelling based methodology introduced in [1] to match these new requirements. Using this analysis pipeline, we provide multiple forecasts for the w CDM parameter constraints that can be expected from stage 3 and stage 4 weak lensing surveys. We consider different survey setups, summary statistics and mass map filters including Starlets. The forecast takes into account the shear bias, photometric redshift uncertainties and the galaxy intrinsic alignment. The impact of baryons on the summary statistics is investigated and the necessary scale cuts are applied in the forecast. We compare the traditional angular power spectrum analysis to two extrema count statistics (peak and minima counts) as well as Minkowski functionals and the Starlet ℓ_1 -norm of the mass maps. In terms of map filters we find a preference for Starlet over Gaussian filters. Our results further suggest that using a survey setup with 10 instead of 5 tomographic redshift bins is beneficial. The addition of cross-tomographic information is found to improve the constraints on cosmology and especially on galaxy intrinsic alignment for all statistics. In terms of constraining power, we find the angular power spectrum and the peak counts to be equally matched for stage 4 surveys, followed by minima counts, the Minkowski functionals and then the Starlet ℓ_1 -norm. Combining different summary statistics significantly improves the constraints and compensates for the constraining power that is lost due to the stringent scale cuts. We identify the most ‘cost-effective’ combination to be the angular power spectrum, peak counts and Minkowski functionals following Starlet filtering.

¹Corresponding author.

Contents

1	Introduction	2
2	Theory	3
2.1	Weak gravitational lensing	3
2.2	Mass mapping	4
2.3	Mass map summary statistics	5
2.3.1	Angular power spectrum	5
2.3.2	Higher order statistics	6
3	Data	10
3.1	Mock survey	10
3.2	COSMOGRID	11
4	Method	13
4.1	Mass map forward modelling	14
4.2	Modelling of systematic effects	15
4.3	Data compression	18
4.4	Emulator	18
4.5	Parameter inference	19
5	Results	19
5.1	Comparison of filter schemes	20
5.2	Comparison of survey designs	21
5.3	Comparison of summary statistics	22
5.4	Galaxy intrinsic alignment	23
5.5	Tomography	24
5.6	Baryons	24
5.7	Fiducial constraints	26
6	Conclusions	30
A	Distribution of the used COSMOGRID simulations	33
B	Fiducial constraints on full wCDM parameter space	33
C	Parameter constraints without scale cuts	33

1 Introduction

Weak gravitational lensing (WL) refers to the observed distortions of the shapes of background galaxies that are caused by the gravitational lensing due to the foreground large scale structure (LSS) of the Universe. While the WL signal from a single galaxy is on the percent-level, the statistical signal from many galaxies exhibits a strong dependence on cosmology. Through the shape measurement of millions of galaxies, WL allows the reconstruction of the projected matter distribution of the local Universe in an unbiased way. Furthermore, the addition of tomographic information enables one to map the evolution of structure formation (see e.g. [2–4] for a review).

Supported by the scientific results of past and ongoing galaxy surveys such as the Canada France Hawaii Telescope Lensing Survey¹ (CFHTLenS) [5], the Kilo-Degree Survey² (KiDS) [6, 7], the Subaru Hyper Suprime-Cam³ (HSC)[8] and the Dark Energy Survey⁴ (DES) [9–11] WL has established itself as a powerful cosmological probe and is listed as one of the major science goals of future large-scale surveys such as the Legacy Survey of Space and Time⁵ (LSST) [12], the Nancy Grace Roman Space Telescope⁶ (NGRST, formerly WFIRST) [13] and *Euclid*⁷ [14].

While the projected matter distribution is well approximated by a homogeneous and isotropic Gaussian random field with zero mean on large scales, the non-linear nature of the gravitational collapse of high-density structures makes the field primarily non-Gaussian on small scales. Past studies relied heavily on two-point statistics such as the the real-space two-point correlation function (see e.g. [9, 15]) or the angular power spectrum (see e.g. [7, 8]) to extract information from the mass maps. Such two-point statistics are sufficient summary statistics for a Gaussian random field with zero mean, but are unable to extract most of the non-Gaussian information on small scales [16, 17]. With the increased resolution of small scale features in upcoming surveys the extraction of non-Gaussian information from the projected matter distribution becomes even more important. Hence, multiple higher order summary statistics were developed in recent years to target this additional non-Gaussian information. Some important examples include three-point statistics [18–20], higher order mass map moments [21–24], Minkowski functionals [25–27], peak counts [28–35], minima counts [36], the ℓ_1 -norm [37], wavelet based methods [38] as well as machine learning based approaches [34, 39–41].

The use of higher order mass map statistics is hindered in practice by the fact that most of them are very difficult to predict from a theoretical framework due to the highly non-linear nature of the gravitational collapse of structures in the late Universe. [1] (hereafter Z21a) developed an analysis pipeline that circumvents this issue by relying on forward-modelling. The statistics are predicted numerically based on a large suite of N-Body simulations. The developed framework was shown to recover the input cosmology when using synthetic weak

¹cfhtlens.org

²kids.strw.leidenuniv.nl

³hsc.mtk.nao.ac.jp/ssp/survey

⁴darkenergysurvey.org

⁵lsst.org

⁶nasa.gov/content/goddard/nancy-grace-roman-space-telescope

⁷sci.esa.int/web/euclid

lensing data. Furthermore, the analysis pipeline was successfully applied to the shape catalog generated from the first three years of data of the DES [42] obtaining state-of-the-art constraints on the structure growth parameter S_8 by [43] (hereafter Z21b).

The goal of this paper is twofold. Firstly, we improve the methodology developed in Z21a and applied to data in Z21b. More specifically we expand the studied parameter space from the matter density Ω_m and amplitude of density fluctuations σ_8 to a full w CDM analysis using the significantly larger N-Body suite COSMOGRID [44], we include a wavelet-based filtering scheme known as the Starlet decomposition [45] and we transition from a Gaussian Process Regressor to a neural network emulator. Secondly, we investigate the forecasted performance of some mass map summary statistics (specifically the angular power spectrum, peak counts, minima counts, Minkowski functionals and the ℓ_1 -norm) in different survey setups. We study how the statistics compare in terms of constraining power and robustness to galaxy intrinsic alignment. Furthermore, the importance of cross-tomographic information, the number of redshift bins and the choice of the mass map filter scheme is investigated for all the different statistics. Using a set of baryon contaminated N-Body simulations, we derive how the statistics are affected by baryonic physics and we derive the scale cuts that are necessary to obtain unbiased results in a stage 4 survey setup. Based on our findings we make suggestions for some analysis choices for a stage 4, full w CDM analysis using higher order statistics. Lastly, we also explore the potential of different combinations of summary statistics.

This paper starts with a short introduction about weak gravitational lensing, mass mapping and mass map statistics in Section 2. In Section 3 the used N-body simulation suite is presented and the generation of the mock shape catalogue is described. Section 4 introduces how we forward model the mass maps and summary statistics for different cosmologies and the parameter inference. We present the findings of this work in Section 5. Lastly, we summarize the main outcomes of this study and make suggestions for future works in Section 6. Further, we show the distribution of the used COSMOGRID simulations in the w CDM parameter space in Appendix A and we include a detailed presentation of the inferred parameter constraints in Appendices B and C.

2 Theory

In the following, we briefly revisit the essentials about weak gravitational lensing and mass mapping. Furthermore, we introduce the summary statistics studied in this work as well as the Starlet decomposition that we employ to filter the maps.

2.1 Weak gravitational lensing

The paths of photons emitted by distant galaxies can be altered by their passage through local deformations of space-time geometry caused by the foreground LSS of the Universe. This effect, that is commonly referred to as gravitational lensing, can lead to distortions in the apparent shapes of the galaxies. As such distortions are typically on the percent level this regime is called weak gravitational lensing (WL). We direct the reader to [2] for a thorough review of the principles of gravitational lensing.

WL leads to two distinct changes of the observed shapes of background galaxies; An isotropic magnification κ of the galaxy size and an anisotropic stretching $\gamma = \gamma_1 + i\gamma_2$ of the ellipticity

of the galaxy. These two quantities can be expressed as a function in spherical coordinates $\kappa(\theta, \varphi)$, $\gamma(\theta, \varphi)$ and are dubbed convergence and cosmic shear, respectively.

Neither the cosmic shear nor the convergence fields are accessible in real-world weak lensing surveys. Instead, only the galaxy ellipticities $e = e_1 + ie_2$ can be measured. They can be regarded as a combination of the intrinsic galaxy shape e_s and the reduced shear g

$$e = g + e_s = \frac{\gamma}{1 + \kappa} + e_s \approx \gamma + e_s, \quad (2.1)$$

where we assumed the weak gravitational limit to approximate $g \approx \gamma$. The intrinsic galaxy shapes e_s are unknown but can be assumed to be random with no preferred orientation, such that $\langle e_s \rangle = 0$, in the absence of galaxy intrinsic alignment. Therefore, the measured galaxy ellipticities e can be understood as noisy measurements of the cosmic shear

$$\gamma_{\text{obs}} = m\gamma + c + e_s, \quad (2.2)$$

where the noise term e_s is often referred to as shape noise. Since the shape noise contribution is typically larger than the cosmic shear signal by about two orders of magnitude, the statistical potency of the signal must be enhanced by averaging over multiple galaxies in the same region of the sky [2]. The shear bias terms are indicated by m (multiplicative shear bias) and c (additive shear bias). Shear bias is a major systematic in weak lensing measurements, that we discuss in Section 4.2. For the remainder of this theoretical introduction we assume $m = 1, c = 0$.

2.2 Mass mapping

The challenge of calculating the convergence signal κ from the noisy, often only partial sky cosmic shear field γ_{obs} is referred to as mass mapping and several methods have been developed in the past to address this problem, some of which are explored in [46]. We follow a direct, analytical formalism developed in [47, 48] that is commonly referred to as the spherical Kaiser-Squires (KS) method. Being defined as spherical fields, the convergence and cosmic shear signals can be decomposed in the basis of spherical harmonics ${}_s Y_{\ell m}(\theta, \varphi)$ with spin-weight s as

$$\gamma(\theta, \varphi) = \sum_{\ell=0}^{\ell_{\text{max}}} \sum_{m=-\ell}^{\ell} {}_2 \hat{\gamma}_{\ell m} {}_2 Y_{\ell m}(\theta, \varphi), \quad (2.3)$$

$$\kappa(\theta, \varphi) = \sum_{\ell=0}^{\ell_{\text{max}}} \sum_{m=-\ell}^{\ell} {}_0 \hat{\kappa}_{\ell m} {}_0 Y_{\ell m}(\theta, \varphi). \quad (2.4)$$

The series are infinite in ℓ and they need to be truncated at an ℓ_{max} in practical applications. We use the `map2alm` routine of the HEALPIX⁸ software [49] to decompose the fields in spherical harmonic space. We use a pixel resolution of `NSIDE` = 1024 with a default $\ell_{\text{max}} = 3 \cdot \text{NSIDE} - 1 = 3071$.

⁸<http://healpix.sf.net>

It can be shown that both fields can be related to the lensing potential $\phi(\theta, \varphi)$ using the covariant derivative $\bar{\partial}$ and its adjoint $\bar{\partial}^\dagger$ through

$$\gamma = \frac{1}{2} \bar{\partial} \bar{\partial}^\dagger \phi, \quad (2.5)$$

$$\kappa = \frac{1}{4} (\bar{\partial} \bar{\partial}^\dagger + \bar{\partial}^\dagger \bar{\partial}) \phi. \quad (2.6)$$

In spherical harmonics space these relations read

$${}_2\hat{\gamma}_{\ell m} = \frac{1}{2} \sqrt{(\ell-1)\ell(\ell+1)(\ell+2)} {}_0\hat{\phi}_{\ell m}, \quad (2.7)$$

$${}_0\hat{\kappa}_{\ell m} = -\frac{1}{2} \ell(\ell+1) {}_0\hat{\phi}_{\ell m}. \quad (2.8)$$

Hence, we can obtain a relation connecting the convergence and cosmic shear fields in harmonic space

$${}_2\hat{\gamma}_{\ell m} = \mathcal{D}_\ell {}_0\hat{\kappa}_{\ell m}, \quad (2.9)$$

where the kernel \mathcal{D}_ℓ is defined as

$$\mathcal{D}_\ell = -\sqrt{\frac{(\ell-1)(\ell+2)}{\ell(\ell+1)}}. \quad (2.10)$$

2.3 Mass map summary statistics

The convergence signal can be decomposed into a curl-free (E-modes) and divergence-free (B-modes) part as $\kappa = \kappa^E + i\kappa^B$ (or in spherical harmonic space ${}_0\hat{\kappa}_{\ell m} = {}_0\hat{\kappa}_{\ell m}^E + i{}_0\hat{\kappa}_{\ell m}^B$). Gravitational lensing only produces an E-mode signal, while systematic effects like galaxy intrinsic alignments and also imperfections in the shear calibration pipeline can give rise to B-modes as well. In the presence of a mask, mode mixing occurs, leading to the production of mixed EB-modes and the leakage of E-modes into the B-mode signal and vice-versa. Hence, we only calculate mass map summary statistics from the E-mode part of κ to constrain cosmology as it is expected to carry most of the cosmological information. We will drop the E superscript in the following. Further, we note that masking effects are included in the numerical predictions of the summary statistics due to the forward-modelling scheme followed in this study and we do not need to correct for such effects.

In the following, we briefly introduce the summary statistics studied in this work and explain how they are measured from the mass maps.

2.3.1 Angular power spectrum

Having the advantage of being accurately predictable from the matter power spectrum using the Limber approximation [50], angular power spectra are used as one of the primary ways to extract information from mass maps in WL studies (see [5, 8, 9, 15, 51–53] for example). We calculate the auto and cross angular power spectra from the tomographic mass maps in the spherical harmonics space as

$$C_{\ell, (i, j)} = \frac{1}{2\ell+1} \sum_{m=-\ell}^{\ell} {}_0\hat{\kappa}_{\ell m, i} \cdot {}_0\hat{\kappa}_{\ell m, j}^*, \quad (2.11)$$

using the HEALPIX routine `anafast` [54]. The indices i and j indicate the tomographic bins. We measure the angular power spectra of the maps using a range of $\ell \in [1, 2048]$ and 25 square-root-spaced bins.

2.3.2 Higher order statistics

Given the decomposition in spherical harmonic space of two tomographic mass maps ${}_0\hat{\kappa}_{\ell m, i}$ and ${}_0\hat{\kappa}_{\ell m, j}$ from two tomographic bins i and j we produce maps as

$$\kappa_{i,j}(\theta, \varphi) = \sum_{\ell=0}^{\ell_{\max}} \sum_{m=-\ell}^{\ell} \sqrt{{}_0\hat{\kappa}_{\ell m, i}} \sqrt{{}_0\hat{\kappa}_{\ell m, j}} {}_0Y_{\ell m}(\theta, \varphi), \quad (2.12)$$

using the HEALPIX routine `alm2map`. Taking $i = j$ results in the reconstruction of the tomographic mass map corresponding to tomographic bin i , while a cross-tomographic map is obtained when choosing $i \neq j$. We utilize a multi-scale approach in this study in order to extract non-Gaussian information from features at different scales. Such an approach was shown to extract more information from the convergence maps compared to a single-scale approach (see [1, 31, 55] for example). Hence, we subsequently filter the maps with a set of filters before the calculation of the higher-order statistics. We consider two types of filters: 1.) A scale-space filtering using a set of Gaussian filters and 2.) a wavelet decomposition using starlet wavelets. In the following, we introduce how these filtered map versions are created from the original map. We follow the methodology and notation introduced in [56].

Conceptually, we produce k filtered versions $c_s(\theta, \varphi)$ of the original map $\kappa(\theta, \varphi)$ by performing convolutions with scaling functions $\phi_s(\theta, \varphi)$, where s runs over the different filter scales

$$c_0 = \phi_0 * \kappa, \quad (2.13)$$

$$c_1 = \phi_1 * \kappa, \quad (2.14)$$

$$\dots \quad (2.15)$$

$$c_k = \phi_k * \kappa. \quad (2.16)$$

In practice, the convolution is executed in spherical harmonic space as

$$\hat{c}_s(\ell, m) = \sqrt{\frac{4\pi}{2\ell+1}} \hat{\phi}_s(\ell, 0) \hat{\kappa}(\ell, m). \quad (2.17)$$

Note that all spherical harmonic coefficients $\hat{\phi}_s(\ell, m \neq 0)$ vanish as we only consider axis-symmetric scaling functions ϕ_s that do not depend on φ . The definition of the low-pass filters

$$\hat{H}_s(\ell, m) = \sqrt{\frac{4\pi}{2\ell+1}} \hat{h}_s(\ell, m) \quad (2.18)$$

$$= \begin{cases} \frac{\hat{\phi}_s(\ell, m)}{\hat{\phi}_{s-1}(\ell, m)} & \text{if } \ell < \ell_s \text{ and } m = 0 \\ 0 & \text{else} \end{cases} \quad (2.19)$$

allows to calculate the smoothed maps $\hat{c}_s(\ell, m)$ in a more efficient, recursive fashion. ℓ_s indicates the characteristic cut-off frequency corresponding to scale s such that

$$\phi_s(\theta, \varphi) = \sum_{\ell=0}^{\ell_s} \hat{\phi}_s(\ell, 0) {}_0Y_{\ell 0}(\theta, \varphi). \quad (2.20)$$

The maps \hat{c}_s can then be calculated recursively as $\hat{c}_s = \hat{H}_s(\ell, m) \hat{c}_{s-1}$.

In the case of the scale-space filtering scheme, we use scaling functions $\phi_s(\theta, \varphi)$ that are Gaussian in real space and characterized by their full-width-at-half-maximum (FWHM). The corresponding spherical harmonic coefficients are

$$\hat{\phi}_s(\ell, 0) = \exp\left(-\frac{1}{2}\ell(\ell+1)\sigma\right) \quad (2.21)$$

where

$$\sigma = \frac{\text{FWHM}}{60} \frac{\pi}{180} \frac{1}{2\sqrt{2\ln(2)}}. \quad (2.22)$$

In our analysis we use 12 such scaling functions with $\text{FWHM} \in [31.6, 29.0, 26.4, 23.7, 21.1, 18.5, 15.8, 13.2, 10.5, 7.9, 5.3, 3.3]$ arcmin. We adapt the same FWHMs as used previously in [1, 31, 43] but we change the smallest scale from 2.7 to 3.3 arcmin. We will refer to this filtering scheme as the GAUSS scheme. The resulting spherical harmonic coefficient $\hat{\phi}_s(\ell, 0)$ are shown in the left-most panel of Figure 1. Note that there is no cut-off scale for the Gaussian filters, resulting in $\ell_s = \infty$.

In the second approach, we extract information from the wavelet decomposition $w_s(\theta, \varphi)$ of $\kappa(\theta, \varphi)$, where the index s runs over a set of different filter scales once again. Having decomposed the original map into smoothed versions c_s as described above the wavelet decomposition can be obtained as

$$w_s(\theta, \varphi) = c_{s-1}(\theta, \varphi) - c_s(\theta, \varphi). \quad (2.23)$$

The wavelet decomposition $w_s(\theta, \varphi)$ of $\kappa(\theta, \varphi)$ can be understood as a version of κ that was smoothed with a band-pass filter $\hat{\psi}_s(\ell, m) = \hat{\phi}_{s-1}(\ell, m) - \hat{\phi}_s(\ell, m)$. The filters $\hat{\psi}_s(\ell, m)$ are commonly referred to as wavelets. Wavelets have emerged as popular and powerful tools in cosmology in the past decades [57] for example for extracting non-Gaussianities from the Cosmological Microwave Background [58–61], reconstructing the primordial power spectrum [62] or reconstruction of WL mass maps [63–66], among other applications. While in principle many functions would make for reasonable scaling function to construct wavelets, Box splines of order 3 have emerged as a very popular choice in astronomy and cosmology [67]. The passage from one resolution to the next is performed through the ‘à trous’ algorithm [68] and they have the advantage of verifying the dilation equation allowing for a fast transformation. Thus, the scaling functions read

$$\hat{\phi}_s(\ell, 0) = \frac{3}{2} B_3\left(\frac{2\ell}{\ell_s}\right), \quad (2.24)$$

$$B_3(x) = \frac{1}{12}(|x-2|^3 - 4|x-1|^3 + 6|x|^3 - 4|x+1|^3 + |x+2|^3). \quad (2.25)$$

The scaling functions are characterized by their cut-off scales ℓ_s . The larger ℓ_s , the more small scale information is included. The isotropic wavelet transform obtained using the above isotropic B_3 -spline scaling functions is also known under the name of starlet transform [45]. It can be fully defined by its symmetric filters from the filter bank and its dictionary is very well adapted to astronomical applications. It has also been shown to be a powerful tool in extracting cosmological information in an ideal, planar setting [37] and to present advantageous characteristics such as a more diagonal covariance matrix in the context of peak counts, compared to Gaussian filters [55].

We consider two different sets of cut-off frequencies for the starlets in this study. Firstly, we use the originally proposed dyadic scheme in which each cut-off frequency ℓ_s can be obtained as $\ell_s = 2\ell_{s-1}$ and the largest cut-off frequency is given by the resolution of the maps as $4 \cdot \text{NSIDE}$ [57]. This results in $\ell_s \in [8, 16, 32, 64, 128, 256, 512, 1024, 2048, 4096]$. We will refer to this filtering scheme as the DYADIC scheme. The wavelet formalism is not restricted to a dyadic spacing of the filters and alternative wavelet transforms that allow filtering at any intermediate scales are possible. Therefore, for the purposes of this study, we also construct a second set of cut-off frequencies $\ell_s \in [1000, 1221, 1491, 1821, 2223, 2715, 3315, 4048, 4943, 6035, 7370, 8999, 10988, 13418, 16384]$ with a larger number of cut-off frequencies and more of them concentrated at smaller scales (the frequencies are still spaced linearly in log space but such that $\ell_s = 1.22\ell_{s-1}$). We expect that this choice of cut-off frequencies leads to an increase in the amount of extracted cosmological information as small-scale structures, that carry most of the non-Gaussian information, are better resolved. We will refer to this filtering scheme as the LOG scheme. We have chosen the largest cut-off frequency of 16384 such that the stacked profiles around local maxima identified from the mass maps are most similar to the ones found for maps smoothed with a Gaussian kernel with FWHM = 3.3 arcmin. This was done to assure that the smallest features accessible in both approaches are approximately of the same scale. The resulting Fourier responses of the wavelets $\hat{\psi}_s(\ell, m)$ corresponding to these two schemes are shown in the middle and right-most plot in Figure 1.

We make the developed software used to calculate the starlet decompositions of the spherical maps in this project publicly available at **eSD**⁹. The core functions of **eSD** are written in C/C++ and taken from **CosmoStat**¹⁰ [69] and **Sparse2D**¹¹ [70]. **eSD** includes an easy-to-use Python wrapper around the just mentioned C++ core routines and is installable out-of-the-box.

In the following, we introduce the higher-order statistics investigated in this study. Namely local extrema (peaks and minima), Minkowski functionals and the starlet ℓ_1 -norm. We calculate all statistics in all three filtering schemes except for the starlet ℓ_1 -norm which is only calculated in the wavelet filtering schemes DYADIC and LOG.

Local extrema The number counts of local maxima (peaks) on pixelized maps as a function of either their convergence or signal-to-noise (SNR) was demonstrated to be an excellent higher-order statistic that is complementary to two-point statistics (see for example [1, 17, 71, 72]) and was previously used to constrain cosmology from observed data (see for example [35, 43, 73]). Initially introduced to detect massive structures from the weak lensing signal, lensing peaks trace overdense regions of the LSS in an unbiased way [74–77].

Targeting the complementary, underdense regions of mass maps, the number counts of local minima offers a promising alternative to peak counts. While the extracted information was demonstrated to be correlated with the information from peak counts, there are some indications that local minima are less susceptible to systematic biases from baryonic physics [1, 36]. Additionally, the study of underdense regions might offer insights into physics beyond the standard model such as modified gravity (see for example [78, 79]).

⁹https://cosmo-gitlab.phys.ethz.ch/cosmo_public/eSD

¹⁰<https://github.com/CosmoStat/cosmostat>

¹¹<https://github.com/cosmostat/sparse2d>

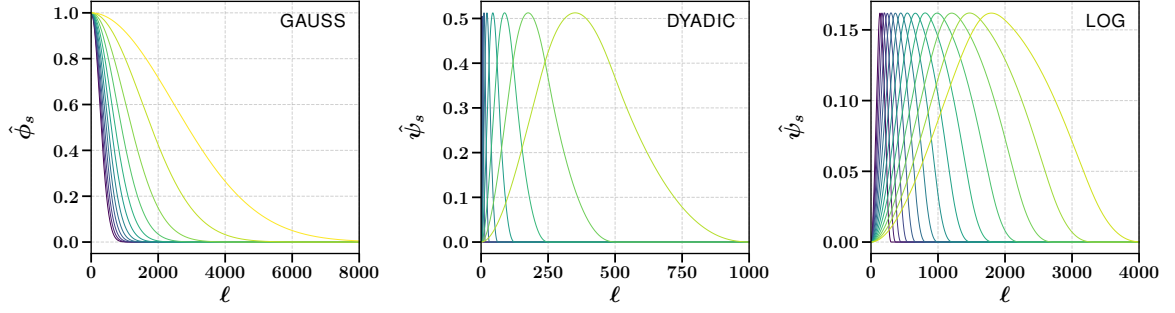


Figure 1. **Left:** The scaling functions used in the GAUSS scheme. These are used to smooth the mass maps before the extraction of information and correspond to Gaussian kernels with FWHM $\in [31.6, 29.0, 26.4, 23.7, 21.1, 18.5, 15.8, 13.2, 10.5, 7.9, 5.3, 3.3]$ arcmin in real space. **Middle:** The starlet wavelets used to filter the mass maps in the DYADIC scheme. The cut-off scales of the filters are $\ell_s \in [8, 16, 32, 64, 128, 256, 512, 1024, 2048, 4096]$. **Right:** The corresponding starlet wavelets used in the LOG scheme with $\ell_s \in [1000, 1221, 1491, 1821, 2223, 2715, 3315, 4048, 4943, 6035, 7370, 8999, 10988, 13418, 16384]$.

We regard a pixel of the filtered mass maps as a peak/minimum if its convergence value is higher/lower than all its neighbouring pixels. Note however, that the definition of a lensing peak/minimum is not unique. Other studies use the local maxima on aperture-mass maps to identify lensing peaks for example [32, 35, 73]. All recorded peaks/minima are then binned as a function of their convergence value into 15 linearly spaced bins. To suppress shot-noise contributions and make the likelihood more Gaussian we adjust the edges of the first and last bins such that at least 30 peaks/minima are found in both of these bins in all simulations. Additionally, we restrict ourselves to peaks with $\text{SNR} \leq 4.0$ (and minima with $\text{SNR} \geq -4.0$) as such strong structures were found to be potentially biased by source clustering [35, 43, 73].

Starlet ℓ_1 -norm Developed by [37], the starlet ℓ_1 -norm was demonstrated to significantly outperform single-scale extrema counts in a planar, ideal setting in terms of constraining power on Ω_m, σ_8 and the sum of neutrino masses. Given a starlet filtered mass map f (being either c_s or w_s depending on the used filter scheme) the starlet ℓ_1 -norm is calculated as

$$\ell_1 = \sum_{u \in B(\text{SNR}_1, \text{SNR}_2)} |f[u]|, \quad (2.26)$$

where we defined the set $B(\text{SNR}_1, \text{SNR}_2) = \{u : \text{SNR}_1 < f[u] < \text{SNR}_2\}$. The ℓ_1 -norm is designed to capture the information in all pixels of the maps and not only at the locations of local extrema. We record the ℓ_1 -norm for each starlet transformed version of the original mass map in the range $\text{SNR} \in [-4.0, 4.0]$ using 15 linearly spaced bins. To the best of our knowledge, this study is the first one to investigate the robustness of the starlet ℓ_1 -norm to galaxy intrinsic alignment, photometric redshift uncertainty and shear bias.

Minkowski Functionals By defining the excursion sets $Q_{\text{SNR}} = \{f : f \geq \text{SNR} \cdot \sigma_f\}$ the Minkowski functionals of a filtered mass map f (being either c_s or w_s depending on the used

filter scheme) can be calculated as a function of SNR as

$$V_0(\text{SNR}) = \frac{1}{Q_{\text{SNR}}} \int_{Q_{\text{SNR}}} \Theta(f(\vec{x}) - \text{SNR} \cdot \sigma_f) dx dy, \quad (2.27)$$

$$V_1(\text{SNR}) = \frac{1}{4Q_{\text{SNR}}} \int_{Q_{\text{SNR}}} \delta(f(\vec{x}) - \text{SNR} \cdot \sigma_f) \sqrt{(\partial_x f)^2 + (\partial_y f)^2} dx dy, \quad (2.28)$$

$$V_2(\text{SNR}) = \frac{1}{2\pi Q_{\text{SNR}}} \int_{Q_{\text{SNR}}} \delta(f(\vec{x}) - \text{SNR} \cdot \sigma_f) \frac{2\partial_x f \partial_y f \partial_x \partial_y f - (\partial_x f)^2 \partial_y^2 f - (\partial_y f)^2 \partial_x^2 f}{(\partial_x f)^2 + (\partial_y f)^2} dx dy, \quad (2.29)$$

where σ_f denotes the standard deviation of the filtered mass map and δ and Θ the Dirac delta and Heaviside-step functions, respectively [80]. We calculate the derivatives numerically on the pixel level. The Minkowski functionals capture the global topology of a continuous, stochastic field and were shown to probe deviations from Gaussianity [81]. The three functionals V_0 , V_1 and V_2 can be interpreted as describing the area, the perimeter and the Euler characteristic of the excursion sets [82]. We measure each Minkowski functional from the mass maps as a function of SNR in the range $[-4.0, 4.0]$ divided in 10 linearly spaced bins.

3 Data

In this section, we explain the production and analysis choices made for the two main ingredients required in this study: 1.) A mock weak lensing shape catalog with realistic galaxy shapes and redshifts, 2.) A large suite of dark-matter-only N-Body simulations covering the studied parameter space.

3.1 Mock survey

We study and compare the performance of different mass map summary statistics in three different scenarios that we dub STAGE 3, STAGE 4 (5 Z-BINS) and STAGE 4 (10 Z-BINS). A summary of the key survey properties of the different setups is presented in Table 1.

We consider a DES-like stage 3 weak lensing shape catalog in the STAGE 3 setup. We assume a survey area of $5'000 \text{ deg}^2$ and a galaxy density n_{gals} of 10 galaxies per arcmin^2 , which corresponds to the values expected for the full DES survey [83]. The positions of the source galaxies on the sky are drawn randomly within the survey area until the target galaxy density is reached. The intrinsic ellipticities e_s of the galaxies are drawn from the probability distribution

$$\text{Prob}(e_s) \propto (e_s + 0.01)^{-4} [1 - \exp(-23e_s^4)], \quad (3.1)$$

and the ellipticity components are obtained as

$$\begin{aligned} e_{s,1} &= \Re[e_s \exp(i\phi)], \\ e_{s,2} &= \Im[e_s \exp(i\phi)], \end{aligned} \quad (3.2)$$

where the angle ϕ is drawn uniformly from the interval $[0, 2\pi[$. This corresponds to the same choice made in Z21a. The functional form of the distribution in Equation 3.1 was proposed by [84] and fit to the observed distribution of galaxy ellipticities measured by [9]. We note that such a mock shape catalog does not reproduce the distribution of galaxy shapes, that is expected to be observed in a real galaxy survey but only the shape noise. Since the mock

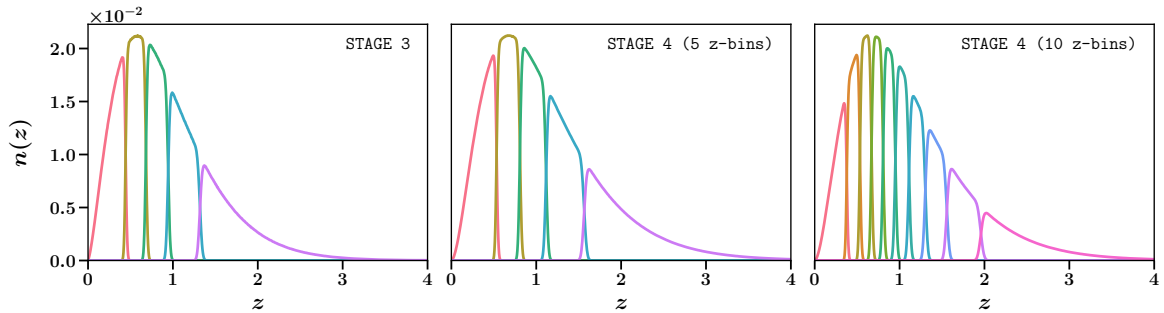


Figure 2. Normalized, tomographic redshift distributions of the source galaxies in the produced mock weak lensing surveys. The three plots show the distributions for the three different survey setups STAGE 3, STAGE 4 (5 Z-BINS) and STAGE 4 (10 Z-BINS) from left to right. The global redshift distributions correspond to Smail distributions.

catalog is only used as a source of shape noise in this study this is sufficient for our purposes and does not affect the results.

The redshifts of the individual galaxies are drawn from a Smail distribution [85]

$$n(z) \propto z^\alpha \exp\left(-\left[\frac{z}{z_0}\right]^\beta\right), \quad (3.3)$$

that is characterized by the three parameters α , β and z_0 . The values chosen for α , β and z_0 for the STAGE 3 setup correspond to the values adopted in Z21a that were fit to the redshift distribution observed by [9], but with z_0 altered to account for the increased survey depth of the completed DES. The galaxies are then subdivided into 5 tomographic bins according to their redshifts, following the scheme introduced in [86]. The used strategy assures that each tomographic bin contains the same number of galaxies. The resulting, tomographic redshift distributions are presented in the left-most plot in Figure 2.

We use the same strategies to produce the mock surveys for the STAGE 4 (5) and STAGE 4 (10) setups, but we change the survey properties to reflect what is expected from a completed stage 4 weak lensing survey. We consider an LSST-like setup and model our mock survey according to the recommendations defined by [87]. Hence, we increase the survey area and the galaxy density n_{gals} to $14'300 \text{ deg}^2$ and 28 galaxies per arcmin^2 (accounting for blending), respectively. The ellipticities of the galaxies are drawn from the same probability distribution as in the STAGE 3 setup. While the global redshift distribution of the galaxies still follows a Smail distribution it is considerably deeper than in the STAGE 3 setup (see Table 1). We consider two different scenarios for the stage 4 setups: STAGE 4 (5 Z-BINS) and STAGE 4 (10 Z-BINS) with the source galaxies being subdivided into 5 and 10 tomographic bins, respectively. The corresponding tomographic redshift distributions are shown in the middle and right-most panels in Figure 2.

3.2 COSMOGRID

In order to accurately predict the mass map statistics at different cosmologies we require a large suite of dark-matter-only N-Body simulations that sample the desired parameter space.

	STAGE 3	STAGE 4 (5 Z-BINS)	STAGE 4 (10 Z-BINS)
Area [deg ²]	5'000	14'300	14'300
n_{gals} [arcmin ⁻²]	10	28	28
# tomo. bins	5	5	10
$n(z)$	$\alpha = 1.5$	$\alpha = 2.0$	$\alpha = 2.0$
	$\beta = 1.1$	$\beta = 0.68$	$\beta = 0.68$
	$z_0 = 0.44$	$z_0 = 0.11$	$z_0 = 0.11$

Table 1. Summary of the key properties of the three different mock survey setups STAGE 3, STAGE 4 (5 Z-BINS) and STAGE 4 (10 Z-BINS). The last row indicates the adapted parameter values for the global Smail distributions from which the galaxy redshifts are drawn.

For this purpose, we use part of the COSMOGRID simulation suite introduced in [44] and previously used successfully to infer cosmology from the KiDS-1000 survey using a Graph Convolutional Neural Network (GCNN) [41]. Initially intended for machine-learning applications the COSMOGRID simulations sample the w CDM parameter space spanned by the total matter density Ω_{m} , baryon density Ω_{b} , amplitude of density fluctuations σ_8 , scalar spectral index n_{s} , Hubble constant H_0 and the equation-of-state parameter of the dark energy component w . The six-dimensional w CDM space is sampled in 2'500 locations with seven fully-independent simulations each. Additionally, each simulation contains three massive neutrino species that assume a degenerate mass-hierarchy with a mass of $m_{\nu} = 0.02 \text{ eV}$ per species. The light neutrino species are modelled as a relativistic fluid in the simulations [88]. The dark energy density Ω_{Λ} was adjusted in each simulation to achieve a flat geometry. The simulations are run using the full-tree, GPU-accelerated N-Body code PKDGRAV3 [89].

The original COSMOGRID simulation suite contains more simulations than needed to reach the precision required for this project and uses very broad priors on the parameters. The sampled parameter space can be divided into a densely sampled inner parameter region (tighter priors) and an outer, more sparsely sampled region. In this study, we use $\sim 25\%$ of the simulations sampling the inner region, which requires us to put tighter priors on the parameters in the inference process but allows us to have a dense sampling of the studied region without having to run a computationally unfeasible number of mass map simulations. The distribution of the resulting 315 locations in the $\Omega_{\text{m}} - \sigma_8$ plane is shown in Figure 3. As we additionally study the intrinsic alignment parameters A_{IA} and η , we need to extend the grid by two additional dimensions. Since the locations of the COSMOGRID simulations are distributed according to a Sobol sequence we can readily extend the dimensionality of the sampled space without losing the sampling properties of the original distribution. The modelling of the intrinsic alignment signal in the simulations is described in Section 4.2. The sampled ranges of all parameters, that also dictate the priors used in the inference process, are listed in Table 2. Note that there is an additional prior in the $\Omega_{\text{m}} - \sigma_8$ plane that is motivated by the degeneracy of the two parameters in weak lensing studies and that is not included in Table 2 but shown in Figure 3 (black box). The distribution of the simulation locations in the full parameter space is presented in Appendix A.

Additionally, we require a large amount of simulations at a fixed cosmology to build the covariance matrices for the different statistics. We use the 200 fiducial simulations of the COSMOGRID suite for this. The location of the fiducial simulations in the $\Omega_{\text{m}} - \sigma_8$ plane is

Parameter	Prior
Ω_{m}	$\mathcal{U}(0.15, 0.45)$
σ_8	$\mathcal{U}(0.5, 1.3)$
$\Omega_{\text{b}} \times 10^2$	$\mathcal{U}(4.0, 5.0)$
n_{s}	$\mathcal{U}(0.93, 1.0)$
H_0	$\mathcal{U}(65.0, 75.0)$
w	$\mathcal{U}(-1.25, -0.75)$
A_{IA}	$\mathcal{U}(-2.0, 2.0)$
η	$\mathcal{U}(-5.0, 5.0)$
$m_i \times 10^2$	$\mathcal{N}(0.0, 0.5)$
$\Delta_{z,i} \times 10^2$	$\mathcal{N}(0.0, 0.5)$

Table 2. Priors used in the inference step. \mathcal{U} denotes a flat prior with the indicated lower and upper bounds, while \mathcal{N} denotes a normal prior with the indicated mean and scale. Note that there is an additional prior in the $\Omega_{\text{m}} - \sigma_8$ plane that is shown in Figure 3. The priors on m and Δ_z follow [92].

indicated by the black star in Figure 3. The fiducial setting corresponds to $\Omega_{\text{m}} = 0.26, \sigma_8 = 0.84, \Omega_{\text{b}} = 0.0493, n_{\text{s}} = 0.9649, H_0 = 67.36, w = -1.0, A_{\text{IA}} = 0.0, \eta = 0.0$.

PKDGRAV3 requires a lookup table of accurate transfer functions that is also used to generate the initial conditions at $z = 99$. This lookup table is calculated using CLASS [90] and transformed into the N-Body gauge using CONCEPT [91]. The particle positions are then evolved forward to $z = 4$ in 70 time steps. Subsequently, another 70 time steps are taken from $z = 4$ to $z = 0$. All time steps are equally distributed in proper time. The remaining precision parameters of PKDGRAV3 were set to their fiducial values. In all simulations a unit box with a side length of 900 Mpc/h filled with 832^3 particles is used. In order to cover the required redshift range up to $z = 3.5$ the unit box is replicated multiple times. We note, that the redshift distribution of the stage 4 survey setups has a small, but non-negligible tail that reaches beyond $z = 3.5$. Hence, we miss some of the galaxies that are expected to be observed in a stage 4 survey. Therefore, the constraining power of a real stage 4 survey might be slightly higher than predicted in this forecast. However, this small discrepancy does not affect the validity of our results.

Using the lightcone mode of PKDGRAV3, spherical particle density maps with a pixel resolution of $\text{NSIDE} = 2048$ are produced. The HEALPIX software is used to pixelize the unit sphere. The resolution of the maps is downgraded to $\text{NSIDE} = 1024$ in the mass mapping step due to memory constraints (see Section 2.2). The baryonic feedback model used to incorporate effects arising from baryonic physics into the simulations additionally requires a halo catalog. At each time step the built in Friend-of-Friend (FoF) halo finder of PKDGRAV3 is used to produce such a catalog identifying halos using a linking length of one fifth of the mean particle separation. We refer the reader to Section 5.6 for details about the baryonification of the simulations.

4 Method

We compare the performance of different higher-order mass map statistics. We do so following a forward modelling approach. For this purpose, we produce realistic spherical mass maps for different cosmologies based on a mock shape catalog and a suite of dark-matter-only N-Body

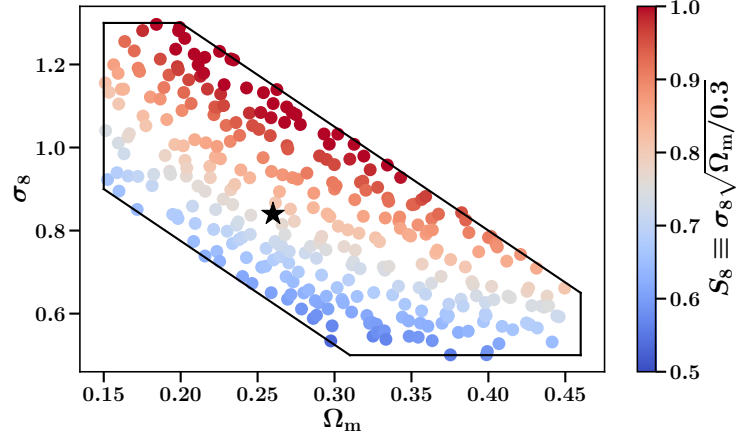


Figure 3. Distribution of the 315 locations of the used COSMOGRID simulations in the $\Omega_m - \sigma_8$ plane. The color indicates the S_8 value at the parameter location. The location of the fiducial simulations is indicated by the star and the black border indicates the prior in the $\Omega_m - \sigma_8$ plane used in the inference step.

simulations. Measuring the different summary statistics from these simulated mass maps allows us to make predictions of the statistics at different cosmologies. In the following, we describe how we simulate realistic mass maps from the N-Body simulations and incorporate systematic effects. Furthermore, we explain how the emulator was set up and how we infer the parameter constraints.

Our methodology builds on [1, 43]. In particular we use the same software and release an updated, more user-friendly version of `estats`¹² that is available for download from the PyPi¹³ as part of this work. The complete codebase used to produce the results presented in this work is publicly available (see NGSF¹⁴) to assure the reproducibility of these results.

4.1 Mass map forward modelling

The `UFalcon`¹⁵ software is used to combine the particle shells obtained from the different PKDGRAV3 simulations into spherical, full-sky mass maps. The `UFalcon` software developed and described in detail in [93] makes use of the Born approximation to avoid full ray-tracing. The Born approximation was shown to be sufficiently accurate for stage 3 as well as stage 4 angular power spectrum analyses [94].

The spherical density contrast shells δ of finite redshift thickness Δ_{z_b} that are obtained from the PKDGRAV3 particle shells are converted into spherical mass maps κ according to

$$\kappa(\hat{n}) \approx \frac{3\Omega_m}{2} \sum_b W_b^{n(z)} \int_{\Delta_{z_b}} \frac{dz}{E(z)} \delta\left(\frac{c}{H_0} \mathcal{D}(z) \hat{n}, z\right), \quad (4.1)$$

where \hat{n} indicates the direction on the unit sphere, H_0 the Hubble constant, c the speed of light, $\mathcal{D}(z_1, z_2)$ is the dimensionless, comoving distance between redshift z_1 and z_2 and the

¹²https://cosmo-gitlab.phys.ethz.ch/cosmo_public/estats

¹³<https://pypi.org/project/estats>

¹⁴https://cosmo-gitlab.phys.ethz.ch/cosmo_public/NGSF

¹⁵<https://pypi.org/project/UFalcon/>

function $E(z)$ is defined as

$$d\mathcal{D} = \frac{dz}{E(z)}. \quad (4.2)$$

The shells are weighted according to the distribution $n(z)$ of the source galaxies in the mock survey using the weights

$$W_b^{n(z)} = \frac{\int_{\Delta_{z_b}} dz \int_z^{z_f} dz' \frac{n(z')}{a(z)E(z)} \frac{\mathcal{D}(0,z)\mathcal{D}(z,z')}{\mathcal{D}(0,z')}}{\left(\int_0^{z_f} dz n(z)\right) \left(\int_{\Delta_{z_b}} \frac{dz}{E(z)}\right)}. \quad (4.3)$$

Subsequently, we cut out an adequate area from the full-sky mass maps using the corresponding mock survey mask. Since none of the studied survey setups covers the whole sky we rotate the full-sky mass maps to obtain multiple mass map realisations from a single PKDGRAV3 simulation (8 for the stage 3 setup and 2 for the two stage 4 setups). Lastly a realistic shape noise signal is added to the simulated mass maps. Since the shape noise signal is added on the shear level the simulated mass maps κ are converted to a shear signal $\vec{\gamma}$ using spherical KS (see Section 2.2).

$$\vec{\gamma}_{\text{sim}} = \vec{e}_{\text{noise}} + \vec{\gamma} = \frac{\sum_{j=1}^{N_{\text{pix}}} \vec{e}_{s,j} \exp(i\phi_j)}{N_{\text{pix}}} + \vec{\gamma}. \quad (4.4)$$

Finally, spherical KS is used once again to transform the fully forward modelled shear signal $\vec{\gamma}_{\text{sim}}$ to a mass map κ_{sim} . The simulated mass map κ_{sim} now includes a realistic, statistically equivalent shape noise signal as the mock survey. Additionally, mode mixing effects caused by the survey mask are included in the simulated mass maps due to the use of spherical KS in the generation procedure and are hence forward propagated into the predictions of the summary statistics.

4.2 Modelling of systematic effects

Weak lensing studies are susceptible to a variety of systematic effects. Leaving these effects unaccounted for can result in significant biases in the values of inferred cosmological parameters in weak lensing studies. A list of the most prominent systematic effects includes baryonic physics, photometric redshift uncertainty, multiplicative shear bias, as well as galaxy intrinsic alignment. We build on the methodology of [1, 43] to include photometric redshift uncertainty, multiplicative shear bias and galaxy intrinsic alignment in our analysis. We do not include baryonic feedback effects in the analysis but we investigate the influence of such effects on the different summary statistics using a set of ‘baronified’ simulations. We also derive the necessary scale cuts that would be needed to alleviate the impact of such effects on the cosmological parameter constraints (see Section 5.6).

Source clustering is another systematic effect that is known to potentially bias the outcomes of weak lensing studies that use information from local extrema (see e.g. [35, 43, 73]). Since the strength of the lensing signal depends on the arrangement of the lens and the source galaxies along the line of sight, the lensing signal in a certain direction on the sky is sensitive to the local distribution of the sources in redshift. The presence of a massive foreground structure like a galaxy cluster alters the local redshift distribution of galaxies in its direction as compared to the average distribution in the field and hence weakens the strength of the lensing signal in that direction of the sky. These local changes in the redshift distribution

that are present in real world data, are not accounted for in our simulations as the positions of the source galaxies are kept fixed on the sky while the distribution of the dark matter varies depending on the seed used in the PKDGRAV3 simulation. This discrepancy can lead to systematic biases when inferring cosmological constraints from observed data and either needs to be forward modelled in the simulations or alleviated by applying appropriate scale cuts. Since we do not have observed data available in this simulation-based study we do not investigate on the strength of this effect, but we apply the same scale cuts as used in Z21b to remove the parts of the data vectors that are potentially affected by this effect, i.e. we do not include peaks with a $\text{SNR} > 4.0$ nor minima with $\text{SNR} < -4.0$.

Furthermore, the presence of massive neutrinos has been shown to lead to a systematic change in the detected number of local maxima from mass maps [55, 95, 96]. Since the sum of the massive neutrino masses is kept constant in the PKDGRAV3 simulations this could potentially lead to biases when applied to observed data. However, since the change is only significant for high SNR peaks ($\text{SNR} \gtrsim 4.0$) the scale cuts already applied to account for source clustering are enough to alleviate the impact of massive neutrinos [96].

In the following we describe how photometric redshift uncertainty, multiplicative shear bias and galaxy intrinsic alignment are incorporated in the analysis.

Photometric redshift uncertainty To realistically forward model a galaxy survey the tomographic distributions of the source galaxies are required. As it is currently not feasible to measure the redshifts of the individual galaxies spectroscopically in large-scale WL surveys the redshift distributions are inferred photometrically. Although a lot of progress was made in the past years, the photometric determination of the redshift distributions remains challenging. Since inaccuracies in these distributions can lead to biases in the inferred cosmological constraints it is vital to take the uncertainty of the redshift distributions into account (see e.g. [97–99]).

We describe the uncertainty of the redshift distributions $n_i(z)$ by a linear shift described by the parameters $\Delta_{z,i}$ as

$$n'_i(z) = n_i(z - \Delta_{z,i}), \quad (4.5)$$

where the index i runs over the tomographic redshift bins considered in the analysis. This method has been used successfully in past studies (see for example [9]). We assume the effect of the parameters $\Delta_{z,i}$ on the cosmological constraints to be independent of cosmology and model their impact at the summary statistic level for each element j of the data vector \vec{d} according to

$$d_j(\theta; \Delta_{z,i}) = d_j(\theta; \Delta_{z,i} = 0)(1 + f_{i,j}(\Delta_{z,i})), \quad (4.6)$$

with θ denoting the remaining, fixed parameters. The functions $f_{i,j}$ are chosen as quadratic polynomials

$$f_{i,j}(\Delta_{z,i}) = c_{i,j}^1 \Delta_{z,i} + c_{i,j}^2 \Delta_{z,i}^2. \quad (4.7)$$

The coefficients of the polynomials are fitted using a set of simulations at the fiducial cosmology in which the injected redshift distributions of the source galaxies were changed according to Equation 4.5. The simulations span the space $\Delta_{z,i} \in [-0.005, 0.005]$ in five linearly spaced points using 4000 simulations per point.

As shown in [100], the impact of redshift errors on cosmological constraints can be cosmology-dependent, especially when varied in combination with intrinsic alignment. In addition, redshift shape errors (e.g. errors of width of the redshift distributions) can also bias constraints and increase the systematic uncertainty. However, with the accuracy of the redshift estimation assumed here, these effects will play only a minor role.

Shear bias The observed changes in the shapes of the source galaxies can be caused by other sources apart from gravitational lensing such as fluctuations in the Earth’s atmosphere, instrumental effects or inaccuracies in the noise model [101–104]. The influence of these effects on the observed shear signal can be modelled by a multiplicative shear bias parameter m and an additive shear bias parameter \vec{c} as

$$\vec{\gamma}_{\text{obs}} = m \vec{\gamma} + \vec{c}. \quad (4.8)$$

The impact of the additive bias on cosmological results is often found to be negligible, thanks to the extensive modelling and correction for shear biases in modern shear calibration pipelines (see e.g. [42]). Hence, we do not include additive shear biases in this forecast. However, we include multiplicative shear bias parameters m_i (i runs over the tomographic bins in the analysis) since even small multiplicative shear biases are expected to significantly alter the outcomes of weak lensing studies (see e.g. [105]). Multiplicative shear bias is implemented in the simulations on the mass map level according to

$$\kappa_{m_i} = (1 + m_i) \kappa_{m_i=0}. \quad (4.9)$$

The effect on the data vectors is modelled in the same way as for the photometric redshift uncertainty using quadratic polynomials that are fitted based on a set of simulations covering $m_i \in [-0.005, 0.005]$ in five linearly spaced points using 4000 simulations per point.

Galaxy intrinsic alignment Cosmic shear measurements rely on the assumption that the intrinsic shapes of galaxies are uncorrelated and average out to zero if the average is taken over a large enough sample of galaxies. However, this assumption is broken in reality due to the gravitational interactions between galaxies with each others as well as the large-scale structure. This effect, that is not accounted for in dark-matter-only simulations, is referred to as galaxy intrinsic alignment (IA) and can introduce strong biases in weak lensing studies [106]. We model the effect of IA on the mass map level using a model developed in [40] that is based on the non-linear intrinsic alignment model (NLA) [107–109]. The method allows to obtain a pure IA signal from the PKDGRAV3 particle shells instead of a mass map by replacing the lensing kernel in Equation 4.3 with an NLA kernel (see Z21a for details). The total mass map including the lensing and IA signal is then simply obtained by adding the two signals together $\kappa = \kappa_{\text{lens}} + \kappa_{\text{IA}}$. The NLA model includes three model parameters: 1.) The amplitude of the overall signal A_{IA} , 2.) a parameter η describing the redshift dependence of the signal, and 3.) a parameter β , describing the dependence of the signal on the luminosity of the galaxy. We fix $\beta = 0$ and only infer A_{IA} and η in the analysis, in accordance with previous studies (see e.g. [9, 43]).

Due to the strong dependency of the IA signal on the underlying cosmology we do not model the IA signal in a cosmology independent fashion like the other systematic effects. Instead we add an IA signal to each of the COSMOGRID simulations by expanding the used Sobol sequence by two dimensions (A_{IA}, η) , drawing an individual IA signal for each simulation.

4.3 Data compression

Depending on the number of filter scales and combined summary statistics the data vectors can contain multiple thousand entries. Although we have 16'000 simulations available at the fiducial cosmology, building the covariance matrix would result in a noisy estimate that could potentially lead to incorrect parameter constraints. Furthermore, we find that the emulator described in Section 4.4 achieves better results when trained on a compressed version of the data vectors instead of the raw data vectors. Therefore, we compress the data vectors using a principal component analysis (PCA) [110] as in Z21a that relies on a singular value decomposition of the data. We use the `sklearn.decomposition.PCA` implementation to perform the PCA and keep enough components to explain at least 99.99% of the variance of the data [111]. The compressed data vectors are whitened to improve the performance of the emulator (see Section 4.4).

4.4 Emulator

Since we only have simulations of the summary statistics available for a finite set of locations in the parameter space, we train an emulator to predict the compressed data vectors for the full parameter space. Hence, we train an artificial neural network to predict the PCA components of the summary statistics from the input cosmological parameters. Since the influence of the nuisance parameters m_i and $\Delta_{z,i}$ is modelled analytically, the network does not have to be trained on these parameters. The network only needs to operate on the eight dimensional parameter space spanned by $\Omega_m, \sigma_8, n_s, H_0, \Omega_b, w, A_{IA}$ and η .

The chosen architecture consists of an input layer, three hidden, fully connected layers with 512 neurons each, as well as an output layer with a linear activation function. All hidden neurons use a Gaussian Error Linear Unit (GeLU) activation function [112], which we found to perform better for this problem than the more commonly used Rectified Linear Unit (ReLU) activation function. The network is trained using the Adam optimiser [113] with a learning rate of 0.0001 over 3000 epochs. The training data is split into mini-batches with a batch size of 32 samples each. We train an individual network for each summary statistics. We use the `tensorflow` software to implement the neural network [114].

Before we trained the networks that are used in the actual analysis, we performed a hyper-parameter optimisation step to choose the learning rate, number of layers, neurons per layer, batch size and the activation function to optimise the performance of the network.

Instead of using a standard mean-squared-error loss function we weigh the contribution of different data vector elements by the estimated variance of the element to put more emphasis on the elements that provide more constraining power

$$L_{\text{loss}} = \sum_{i=0}^n \frac{(y_{i,\text{true}} - y_{i,\text{pred}})^2}{\sigma_i^2}. \quad (4.10)$$

The predicted data vector is indicated by y_{pred} and the true one by y_{true} . The sum runs over all n elements in the data vector and σ_i stands for the estimated standard deviation of the i -th element of the data vector at the fiducial cosmology.

To assess the performance of the emulator we select 20 randomly chosen points from the original set of 315 parameter points that are contained in the convex hull of the remaining points as the validation set. The validation loss is monitored during the training on the

remaining data along with the training loss to check that the network does not overfit to the training data. We train the final networks on the whole data set due to the small number of simulations available. Hence, the obtained validation loss serves as an upper bound for the validation loss of the final network.

We judge the accuracy of the emulators as being adequate for this forecast study. However, we stress that in case of an application to real data it would be favourable to use the whole COSMOGRID simulation suite for the training. Due to the many different summary statistics and survey setups probed in this analysis this was computationally not feasible in this work.

4.5 Parameter inference

We infer the posterior distributions of the cosmological parameters of the w CDM model as well as the NLA model parameters A_{IA} and η given a mock measurement of the summary statistics \vec{y} using a standard Bayesian inference approach. Hence, we estimate the posterior distribution

$$p(\vec{\theta}|\vec{y}) \propto \mathcal{L}(\vec{y}|\vec{\theta})\pi(\theta), \quad (4.11)$$

where $\vec{\theta}$ includes the w CDM, NLA, multiplicative shear bias and the redshift uncertainty parameters. The prior π on the parameters is dictated by the size of the space that is covered by the simulations. The priors on the individual parameters are listed in Table 2. We assume the likelihood of the data to be Gaussian and we apply the same corrections as in Z21a, Z21b to account for the uncertainty in the estimate of the covariance matrix as well as the simulated data vectors used to train the emulator [115, 116]

$$\mathcal{L}(\vec{y}|\vec{\theta}) \propto \left(1 + \frac{N_{\theta}}{(N_{\theta} + 1)(N_{\text{fid}} - 1)}Q\right)^{-N_{\text{fid}}/2}, \quad (4.12)$$

with

$$Q = (\vec{y} - \hat{\vec{y}}(\vec{\theta}))^T \hat{\Sigma}^{-1} (\vec{y} - \hat{\vec{y}}(\vec{\theta})).$$

In the above, $\hat{\Sigma}$ denotes the estimate of the covariance matrix built from the $N_{\text{fid}} = 16'000$ data vector realisations at the fiducial cosmology and $\hat{\vec{y}}(\vec{\theta})$ the estimate of the data vector at a parameter location $\vec{\theta}$ estimated from $N_{\theta} = 560$.

We use the Markov Chain Monte Carlo (MCMC) sampler `emcee` [117] to efficiently sample from the posterior distributions using 25 walkers per parameter (450 for the two setups with five tomographic bins and 700 for STAGE 4 (10 Z-BINS)) with a chain length of 100'000 per walker.

5 Results

We present a range of comparisons of the parameter constraints that we derived using the summary statistics emulators described in Section 4.4 and the parameter inference procedure outlined in Section 4.5. We start by comparing the three different survey setups and the three different filter schemes for the higher order statistics without applying any additional scale cuts. Subsequently, we study the impact of baryonic physics on the different statistics and present the necessary scale cuts for three different baryonic models. We forecast realistic constraints for a stage 4 setup using the derived scale cuts and report on the importance of galaxy intrinsic alignment, cross-tomographic information content, and the potential of

combining different summary statistics.

It was demonstrated by [41] that the angular power spectra measured from the COSMOGRID simulations reproduce the predictions of the theory code PYCCL¹⁶ [118] well for $\ell \gtrsim 20$. Hence, we do not use the lowest two ℓ -bins in the analysis, effectively applying a lower scale cut of $\ell > 20$. For consistency, we also remove the first 4 wavelet filter scales in the DYADIC scheme in the fiducial analysis setting since they nearly exclusively contain modes with $\ell < 20$. Since the non-Gaussian information content on such large scales is expected to be very small this does not significantly alter the results. We do not modify the LOG scheme since none of its filters contain a significant portion of $\ell < 20$ modes. On the other hand, we include all modes $\ell \leq 2048$ in the fiducial angular power spectra analysis. This is approximately in concordance with the scales accessed by the higher order statistics. This is based on the observation that applying the smallest filter of the GAUSS scheme (FWHM=3.3 arcmin) to a mass map leads to a $\sim 50\%$ drop in power at $\ell = 2048$.

As the primary measure for the constraining power we use the Figure of Merit (FoM) that we calculate from the parameter space covariance matrix $\Sigma_{\vec{\theta}}$ according to

$$FoM(\vec{\theta}) = (|\hat{\Sigma}_{\vec{\theta}}|)^{-1/n}. \quad (5.1)$$

The parameter space covariance matrix is estimated from the MCMC chains and n indicates the dimensionality of the parameter space. We calculate the FoM in the subspace that is most constrained by weak lensing measurements, namely the space spanned by Ω_m, S_8 and w_0 (hence setting $n = 3$ and marginalising over the remaining parameters). Furthermore, we also compare the widths of the 1D posterior distributions on these three parameters.

5.1 Comparison of filter schemes

We start by comparing how the different higher order statistics perform depending on the used filter scheme (i.e. GAUSS, LOG, and DYADIC).

A visual comparison between the w CDM constraints obtained from the angular power spectrum analysis and the higher order statistics analyses using the most favourable filter scheme (LOG) is presented in Figure 4. A tabular comparison in terms of FoM and 1D parameter constraints can be found in Table 6 in Appendix C. Firstly, we notice that the DYADIC filter scheme is outperformed by the other two schemes for all summary statistics. This is not surprising given that most of the filters in the DYADIC scheme focus on large scales on which the mass maps are close to a Gaussian random field. We also note that the DYADIC scheme was originally designed for mass map reconstruction routines and not for the extraction of non-Gaussian information from the maps and is therefore not expected to be necessarily optimal for our analysis and its relevant scales.

Comparing the GAUSS and wavelet LOG schemes we find a slight but consistent preference for the wavelet scheme. From Figure 1, we observe that the LOG filters are more concentrated on small scales and contain less large scale modes compared to the GAUSS filters that act as low-pass filters. We suspect that this leads to better resolution of the small scale features and hence to more information extracted from the maps.

¹⁶<https://github.com/LSSTDESC/CCL>

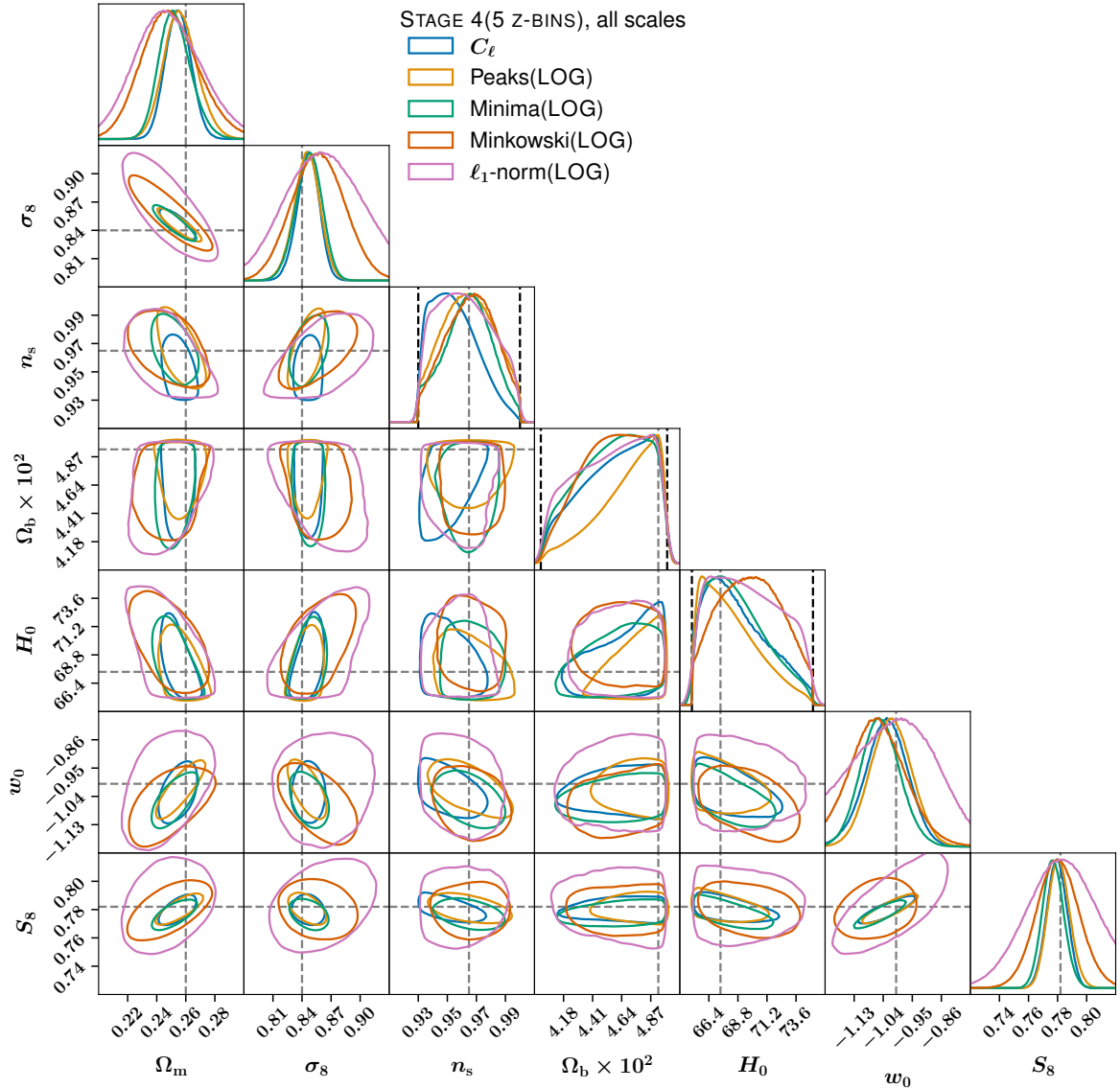


Figure 4. Constraints on the full w CDM parameter space as found in the STAGE 4 (5 z-BINS) survey setup using the most favourable filter scheme for the higher order statistics (namely the LOG scheme). No additional scale cuts were applied. The contours show the 68% confidence regions. The dashed grey lines are located at the true parameter values. We indicate the prior boundaries using a black dashed line in the panels showing the 1D constraints, if the constraints are restricted by the prior.

Based on these observations, we limit the discussion for each statistic to the best case scenario, namely the LOG scheme, in the following investigations.

5.2 Comparison of survey designs

We compare how the constraining power of the different statistics changes with the survey design. The numerical results are again included in Table 6 in Appendix C. All statistics profit greatly from the transition from stage 3 to stage 4 (STAGE 3 \rightarrow STAGE 4 (5 z-BINS)), as expected given the increase in survey area, redshift depth and source galaxy number density.

Table 3. Uncertainties of the 1D-posterior distributions of the three most constrained w CDM parameters Ω_m , S_8 and w_0 as well as the galaxy intrinsic alignment amplitude A_{IA} and the Figure of Merit (FoM). All scales are included in the analysis. We also include the results of an analysis with fixed galaxy intrinsic alignment parameters ($A_{IA} = 0, \eta = 0$), as well as an analysis without cross-tomographic information. The uncertainties are reported as the standard deviations of the 1D posteriors. The remaining w CDM parameters are prior dominated and not listed here. We include the relative change of the values when IA or the cross-bins are not considered as compared to the baseline results in brackets.

Statistic	$FoM(\Omega_m, S_8, w_0)$	$\sigma(\Omega_m) \times 10^2$	$\sigma(S_8) \times 10^2$	$\sigma(w_0) \times 10^2$	$\sigma(A_{IA}) \times 10$
STAGE 4 (5 Z-BINS), all scales					
C_ℓ	8413 (-)	0.871 (-)	0.69 (-)	6.57 (-)	0.72 (-)
Peaks (LOG)	8936 (-)	1.15 (-)	0.747 (-)	6.35 (-)	1.6 (-)
Minima (LOG)	8195 (-)	1.1 (-)	0.731 (-)	6.1 (-)	1.65 (-)
Minkowski (LOG)	2347 (-)	1.39 (-)	2.11 (-)	3.58 (-)	2.76 (-)
ℓ_1 -norm (LOG)	744 (-)	2.34 (-)	2.54 (-)	11.7 (-)	6.88 (-)
STAGE 4 (5 Z-BINS) no IA, all scales					
C_ℓ	10943 (+30%)	0.673 (+22%)	0.542 (+21%)	5.38 (+18%)	-
Peaks (LOG)	13302 (+48%)	0.872 (+24%)	0.598 (+19%)	5.49 (+13%)	-
Minima (LOG)	11348 (+38%)	0.857 (+21%)	0.602 (+17%)	5.24 (+14%)	-
Minkowski (LOG)	3034 (+29%)	1.17 (+19%)	1.82 (+14%)	3.55 (+1%)	-
ℓ_1 -norm (LOG)	934 (+25%)	2.69 (-14%)	1.99 (+21%)	9.65 (+17%)	-
STAGE 4 (5 Z-BINS) no cross-bins, all scales					
C_ℓ	4959 (-41%)	1.27 (-45%)	0.899 (-30%)	8.85 (-34%)	3.82 (-430%)
Peaks (LOG)	4672 (-47%)	1.51 (-30%)	1.09 (-46%)	9.22 (-45%)	3.28 (-104%)
Minima (LOG)	4794 (-41%)	1.39 (-26%)	0.97 (-32%)	7.73 (-26%)	2.98 (-81%)
Minkowski (LOG)	518 (-77%)	3.22 (-132%)	3.04 (-44%)	13.4 (-275%)	9.16 (-232%)
ℓ_1 -norm (LOG)	276 (-62%)	4.93 (-110%)	3.98 (-56%)	12.4 (-5%)	9.26 (-34%)

Additionally, we find that an increase in the number of tomographic redshift bins leads to a further increase in constraining power that is observed for all statistics (STAGE 4 (5 Z-BINS) \rightarrow STAGE 4 (10 Z-BINS)). We take this as an indication that the additional tomographic information can compensate for the increased shape noise in the maps caused by the lower galaxy number density per bin.

For brevity, we restrict all further investigations to the fiducial survey setup STAGE 4 (5 Z-BINS) in the following sections. We decide to use the STAGE 4 (5 Z-BINS) setup over the STAGE 4 (10 Z-BINS) setup, as we expect the results to be the same conceptually, but we are able to run more tests using the STAGE 4 (5 Z-BINS) setup due to the significantly shorter data vectors (15 compared to 55 different tomographic bin combinations). This choice is therefore motivated by computational feasibility.

5.3 Comparison of summary statistics

The order of the statistics with respect to constraining power is found to be peak counts, angular power spectrum, minima counts, Minkowski functionals and the ℓ_1 -norm in descending order (see Table 3 and Table 6 in Appendix C). We present the constraints in the full w CDM parameter space in Figure 4. We find very similar constraints for peak and minima counts with the peaks slightly outperforming the minima as it was also found in previous studies (see e.g. [36]).

While our results regarding the ℓ_1 -norm seem at odds with the findings of [37], where the ℓ_1 -norm outperforms extrema counts as well as the angular power spectrum, we note that our study differs from [37] in multiple aspects. Firstly, the choices of scales in this study differ from [37]. [37] study much smaller scales down to 1.6 arcmin that contain large amounts of non-Gaussian information, while we are limited by the pixel resolution of 3.3 arcmin. The chosen number and selection of cosmological and systematics parameters differ as well; We include all six w CDM parameters as well as systematics parameters describing galaxy intrinsic alignment, photometric redshift uncertainty and multiplicative shear bias. On the other hand, [37] do not include any systematics and limit the cosmological parameters to Ω_m, A_s and the sum of neutrino masses (which is fixed in this study). Lastly, we use a spherical approach covering the whole survey area at once, while [37] used small, planar patches with an area of 12.25 deg^2 from which the covariance matrix is estimated and scaled by $f_{\text{patch}}/f_{\text{survey}} = 12.25 \text{ deg}^2 / 15000 \text{ deg}^2 \approx 8.2 \times 10^{-4}$. We believe such a scaling to be appropriate for extrema count statistics, but might be ill suited for topological summary statistics like Minkowski functionals or the ℓ_1 -norm. The scaling relies on the assumption that each patch contributes an equal amount of information that is independent from the remaining patches. This holds approximately true in the case of the extrema counts, where the number of such features does not vary significantly with the position on the sky and each peak/minimum is, to first order, independent of the the peaks/minima in patches that are sufficiently far away. For summary statistics like Minkowski functionals or the ℓ_1 -norm that aim at capturing the global topology of the mass maps the information provided by the different patches can be highly correlated, with each patch providing an estimate of the same underlying topology. Hence, the used upscaling of the covariance matrix could potentially lead to an overestimation of the constraining power of the topological summary statistics compared to the extrema counts. However, the confirmation of this effect requires further investigation that is outside of the scope of this work.

The Minkowski functionals are outperformed by the extrema statistics in our study. While this agrees with the findings of Z21a, other studies find constraints using Minkowski functionals that rival or even outperform the extrema count statistics constraints [36]. However, given the differences of the two studies, similar arguments as for the ℓ_1 -norm apply.

5.4 Galaxy intrinsic alignment

We investigate the impact of galaxy intrinsic alignment on the different summary statistics by comparing the fiducial results to an analysis in which we fixed the galaxy intrinsic alignment parameters ($A_{\text{IA}} = 0$ and $\eta = 0$). The numerical results are included in Table 3. All statistics gain significantly in constraining power when galaxy intrinsic alignment is not considered in the analysis. We take this finding as an indication that none of the studied statistics is significantly robust to galaxy intrinsic alignment at the stage 4 level. The angular power spectrum constrains A_{IA} the most, but also the extrema counts yield good constraints. None of the statistics can significantly constrain the redshift dependence of the galaxy intrinsic alignment signal η . Again, the strongest constraints are provided by the angular power spectrum. We find a slight tendency for the Minkowski functionals and the ℓ_1 -norm to be less affected by galaxy intrinsic alignment compared to the other statistics.

5.5 Tomography

We investigate how much the cross-bins (e.g. 1x2, 1x3, ...) contribute to the total constraining power for the different statistics. We do so by running a set of analyses in which we do not consider the cross-bins but only the auto-bins. Table 3 presents a comparison of the resulting constraints compared to the fiducial results. We find that all summary statistics significantly profit from the additional cross-tomographic information. Most importantly, we find that the additional information contributes primarily to constraining galaxy intrinsic alignment. Without the cross-tomographic information the constraints on A_{IA} worsen. This also negatively affects the cosmological constraints partially due to the strong correlations between A_{IA} and the cosmological parameters (most notably S_8). The effect is more significant for the statistics that constrain galaxy intrinsic alignment stronger in the first place. Hence, we record a stronger impact for the angular power spectrum and the extrema counts.

5.6 Baryons

The presence of baryonic matter in cosmological simulations was demonstrated to significantly alter the distribution of matter on small scales (see e.g. [119–121]). Hence, baryonic effects have also been shown to affect weak lensing statistics such as the angular power spectrum (see e.g. [122]), as well as peak and minima counts (see e.g. [36, 123]) and Minkowski functionals [124]. Baryonic effects can be included on the level of the matter power spectrum using for example HMCODE [125]. A potential way to include baryonic effects into our simulations would be to run hydrodynamical simulations. However, given that the modelling of baryonic effects, such as active galactic nuclei (AGN) feedback or stellar winds, requires the resolution of very small scales, running such simulations is computationally unfeasible for our analysis. An alternative approach was demonstrated by [126], who trained neural networks to learn to infer the distribution of gas from a given dark matter distribution. Another way to incorporate baryons into such analyses was explored by [41], who used an extension of the *baryonification model* developed in [122, 127, 128] to the shell level. Using the same method as [41] would require to increase the dimensionality of the sampled parameter space by another two parameters resulting in a very sparse sampling given the fixed number of simulations used in this study. While we hope to explore the full integration of baryons in a future study in which a larger fraction of the COSMOGRID simulations can be used, this was not computationally feasible in this work due to the large number of different survey and filter scheme configurations being probed.

Instead, we explore the impact of baryons on the different summary statistics by deriving the necessary scale cuts for each individual statistic for the fiducial STAGE 4 (5 Z-BINS) setup. To do so, we follow the same approach previously used by Z21b. We derive the scale cuts by studying the shift of the cosmological constraints, that is observed when swapping a mock measurement data-vector obtained from one of the simulations at the fiducial cosmology with a data-vector obtained from a baryonified version of the same base simulation with the same initial conditions. The baryonification was achieved by shifting the positions of the particles in the simulation around massive halos leading to a modification of the halo profiles to resemble realistic profiles including the gas, central galaxy and a collisionless dark matter component (see [122, 127, 128] for details). We use the same criterion for the scale cuts as Z21b, requiring that the projected constraints in the $\Omega_m - S_8$ plane do not shift by more than 0.3σ when including baryons. The shift in the constraints is quantified using the

Table 4. We present the derived scale cuts for the different summary statistics as found for the STAGE 4 (5 Z-BINS) survey setup. The table includes the scale cuts for the three different baryonification models A-avrg, B-avrg and C-avrg (see Table 2 in [128] for details). B-avrg corresponds to the best-guess model.

Statistic	A-avrg	B-avrg	C-avrg
STAGE 4 (5 Z-BINS)			
C_ℓ	$\ell \leq 577$	$\ell \leq 495$	$\ell \leq 350$
Peaks (LOG)	$\ell_s \leq 3315$	$\ell_s \leq 3315$	$\ell_s \leq 3315$
Minima (LOG)	$\ell_s \leq 3315$	$\ell_s \leq 3315$	$\ell_s \leq 3315$
Minkowski (LOG)	$\ell_s \leq 6035$	$\ell_s \leq 3315$	$\ell_s \leq 2223$
ℓ_1 -norm (LOG)	$\ell_s \leq 16384$	$\ell_s \leq 1491$	$\ell_s \leq 1491$

`tensiometer` software developed by [129–131]. Contrary to Z21b, who derived scale cuts using a single baryonification model, we use three different baryon contaminated simulations at our fiducial cosmology that correspond to the models A-avrg, B-avrg and C-avrg (see Table 2 in [128]) and derive the scale cuts for each model. B-avrg corresponds to the best-guess model, while the models A-avrg and C-avrg potentially under- and overestimate the impact of baryons. We demonstrate how the fiducial data vector changes for the different statistics when the baryonification is applied to the simulations in Figure 5. We find the angular power spectrum at high multipoles ($\ell > 500$) to be affected the most, with deviations reaching up to $\sim 7\sigma$ for $\ell > 1500$. For the extrema count statistics, we find the peak and minima counts to be affected similarly by the baryons with deviations reaching $\sim 5\sigma$ for high SNR peaks and low SNR minima, respectively. It was found by [36] that the minima counts are more resilient to baryons compared to the peak counts, which seems to be at odds with our findings. However, this only holds true if the high SNR tail of the peak counts is included in the comparison. Hence, this effect is not recorded in our analysis since we restrict ourselves to peaks with $\text{SNR} \leq 4$ and minima with $\text{SNR} \geq -4$. While the topological summary statistics (Minkowski functionals and ℓ_1 -norm) appear to be affected less by baryons, one should take into account that their constraining power is also significantly lower, which relativizes their apparent resilience to baryonic effects.

The derived scale cuts for the different summary statistics are presented in Table 4. The imposed scale cuts are more restrictive compared to earlier studies like Z21b due to the increased constraining power of the STAGE 4 (5 Z-BINS) setup. We note that the very restrictive cuts for the ℓ_1 -norm originate primarily from a strong shift in Ω_m . A change in the criterion used to derive the cuts (e.g. considering the shift in S_8 only) could potentially change these results.

In the following, we apply the B-avrg scale cuts following [128] that propose the B-avrg model as the best-guess model.

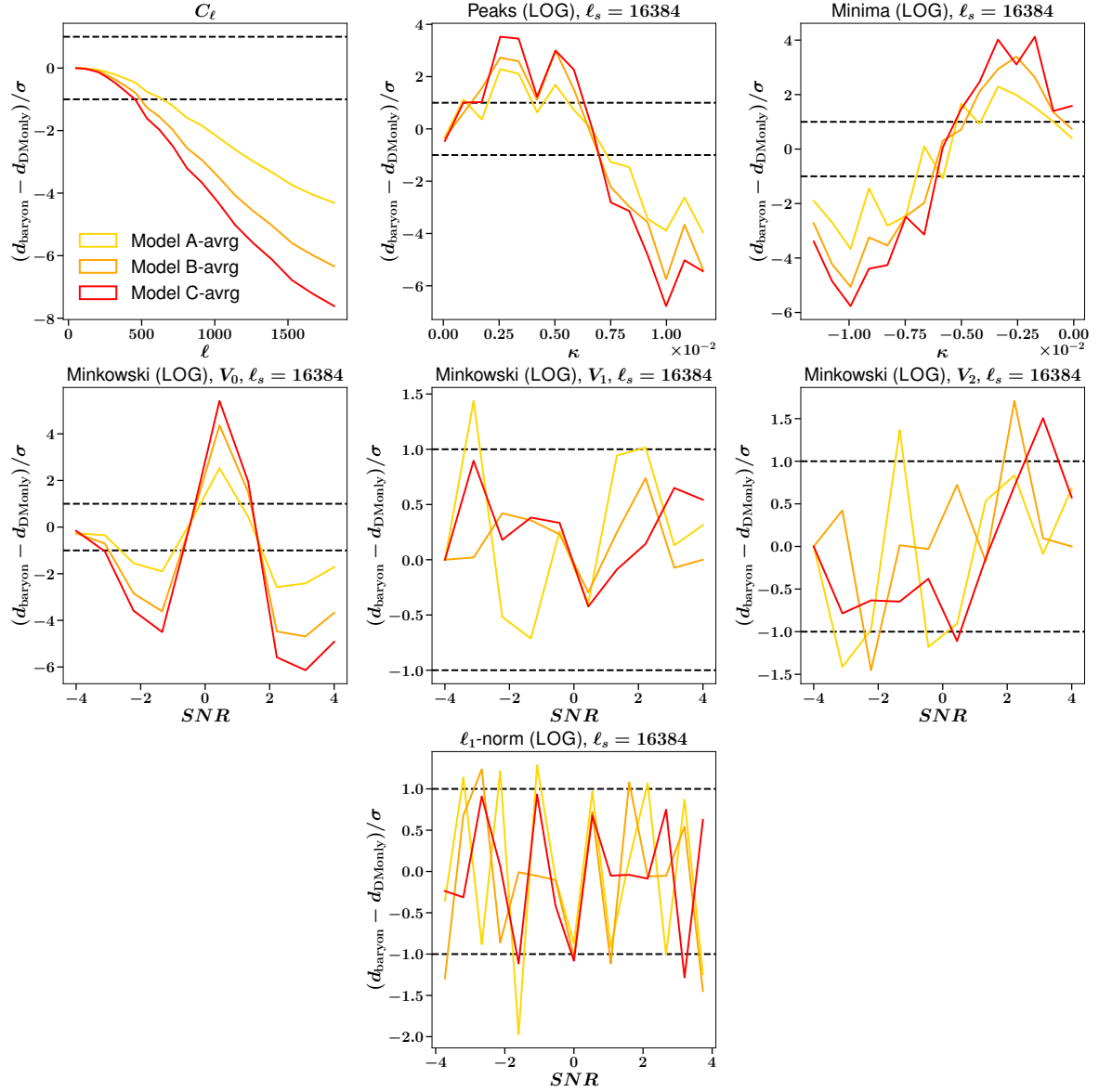


Figure 5. We present how the summary statistics change due to baryonic physics. Each panel shows the relative change of one of the statistics caused by baryonifying the underlying simulation using one of the three baryonic models (A-avrg, B-avrg and C-avrg). We only present the change of the statistics for the 5x5 tomographic bin combination of the STAGE 4 (5 Z-BINS) setup. For the higher order statistics the smallest scale ($\ell_s = 16384$) is used. The relative changes are normalized by the standard deviation in each data bin that is estimated from the diagonal of the covariance matrix at the fiducial cosmology. The dashed, black lines indicate the 1σ level.

5.7 Fiducial constraints

We present the fiducial constraints of our analysis. These constraints are tailored to represent a realistic forecast of the cosmological constraints that can be expected from a stage 4 analysis. We include the most significant weak lensing systematics (galaxy intrinsic alignment, multiplicative shear bias and photometric redshift uncertainty). Realistic scale cuts

are applied to prevent significant biases from unmodelled baryonic physics. The presented constraints are based on the results presented in the previous sections. Hence, we choose the following fiducial setup:

- Filter scheme for the higher-order statistics: LOG
- Survey setup: STAGE 4 (5 Z-BINS)
- Scale cuts: Model B-avrg cuts

Individual statistics The fiducial constraints on the most constrained w CDM parameters (Ω_m, σ_8 and w_0) are displayed in Figure 6, jointly with the constraints on S_8 and A_{IA} . Additionally, the constraints in the full w CDM parameter space are presented in Figure 9 in Appendix B. The numerical results are included in Table 5. The strength of the constraints is strongly diminished by the scale cuts as compared to the results without cuts (see Table 3). The FoM is reduced by a factor of ~ 2 -3 for the angular power spectrum, extrema counts and the Minkowski functionals. The loss is even greater for the ℓ_1 -norm due to the more restrictive scale cuts. We take this significant degradation of the constraints as a strong indication that a full baryonic treatment should be included in a stage 4 weak lensing survey analysis for all summary statistics in order to avoid restrictive scale cuts and to fully realize the potential of all statistics. The ordering of the summary statistics with constraining power is modified compared to the analysis without cuts, with the angular power spectrum now slightly outperforming the peak counts. It is noteworthy that the extrema counts still provide constraints that are comparable to the angular power spectrum although most of the non-Gaussian information on small scales was removed from the data vectors by the scale cuts.

Combined statistics We explore different combinations of the higher order mass map statistics with the angular power spectrum. It was previously demonstrated that such combinations bear the potential to break degeneracies between parameters [132] and strongly constrain cosmology thanks to the different kinds of features and information that is extracted by the different statistics (see for example [32, 43, 73, 133]). Additionally, the statistics react differently to noise and systematic effects, which can improve the robustness of the constraints when combining the statistics Z21a. We list the numerical results for the probed combinations in Table 5. Additionally, we present a selection of the constraints in Figure 7. The corresponding constraints of the full w CDM parameter space are presented in Figure 10 in Appendix B.

From our findings, we conclude that already the combination of the angular power spectrum with a single higher order mass map statistic significantly increases the constraining power. Adding either peak counts or Minkowski functionals is found to be more favourable than minima counts or the ℓ_1 -norm. We note that the constraints on galaxy intrinsic alignment are barely improved by the addition of the higher order mass map statistics but are completely dominated by the angular power spectrum. In turn, the cosmological constraints tighten up significantly thanks to the higher order map statistics that are now more constraining on cosmology due to the galaxy intrinsic alignment parameters being strongly constrained by the angular power spectrum. Further, we notice that if only a single higher order statistic can be added to the angular power spectrum the addition of the Minkowski functionals is the most favourable, indicating that the topological information probed by the Minkowski

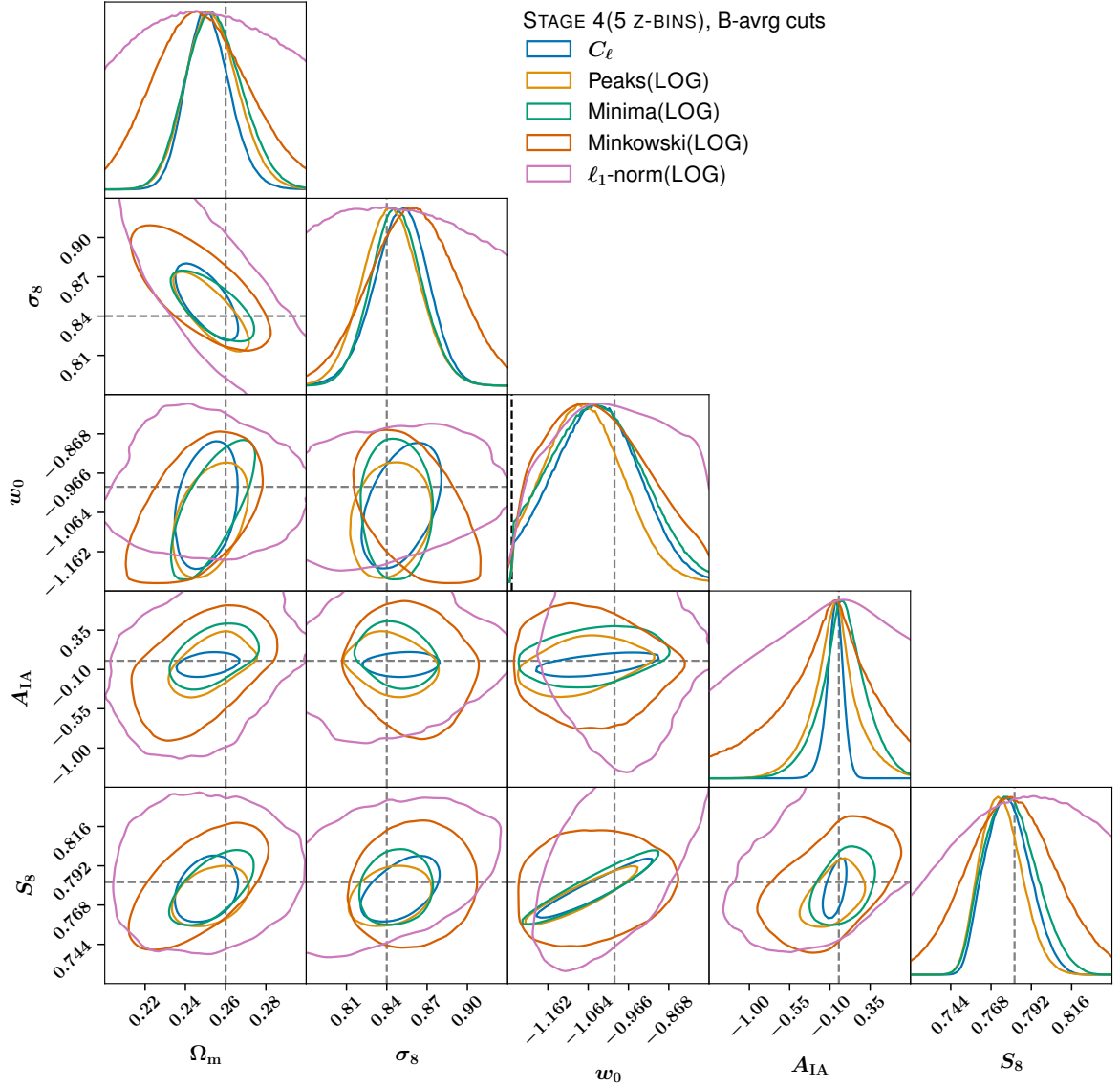


Figure 6. Fiducial constraints on Ω_m, σ_8, w_0 and S_8 as well as A_{IA} for the individual summary statistics. The presented constraints are derived for the STAGE 4 (5 Z-BINS) survey setup using the most favourable filter scheme for the higher order statistics (namely the LOG scheme). The best-guess model B-avrg scale cuts are applied (see Table 4). The presented contours indicate the 68% confidence regions. The dashed grey lines are located at the true parameter values. We indicate the prior boundaries using a black dashed line in the panels showing the 1D constraints, if the constraints are restricted by the prior.

functionals is more independent from the angular power spectrum information than the information probed by the extrema counts.

Adding the minima counts on top of the peak counts further improves the constraining power. On the other hand, adding the ℓ_1 -norm to the Minkowski functionals does not improve the constraints appreciably. From this observation, we conclude that the Minkowski functionals already include nearly all of the information captured by the ℓ_1 -norm. We account this to the

Table 5. The uncertainties of the 1D-posterior distributions of the three most constrained w CDM parameters Ω_m , S_8 and w_0 as well as A_{IA} and the Figure of Merit (FoM) for the fiducial setup. The B-avg model scale cuts were applied. The uncertainties are reported as the standard deviations of the 1D posteriors. We include the relative change of the values in comparison to the angular power spectrum results in brackets.

Statistic	$FoM(\Omega_m, S_8, w_0)$	$\sigma(\Omega_m) \times 10^2$	$\sigma(S_8) \times 10^2$	$\sigma(w_0) \times 10^2$	$\sigma(A_{\text{IA}}) \times 10$
STAGE 4 (5 Z-BINS), B-avg cuts					
C_ℓ	3921 (-)	1.1 (-)	1.27 (-)	9.78 (-)	0.941 (-)
Peaks (LOG)	3362 (-14%)	1.3 (-18%)	1.21 (+4%)	8.99 (+7%)	2.74 (-191%)
Voids (LOG)	3039 (-22%)	1.39 (-26%)	1.49 (-17%)	10.6 (-8%)	2.68 (-185%)
Minkowski (LOG)	680 (-82%)	2.43 (-121%)	2.76 (-117%)	11.9 (-21%)	6.42 (-582%)
ℓ_1 -norm (LOG)	160 (-95%)	6.06 (-451%)	6.86 (-440%)	13.4 (-36%)	9.84 (-945%)
C_ℓ +Peaks(LOG)	8959 (+128%)	0.776 (+29%)	0.836 (+34%)	6.32 (+35%)	0.808 (+14%)
C_ℓ +Voids(LOG)	8171 (+108%)	0.808 (+26%)	0.936 (+26%)	6.63 (+32%)	0.894 (+4%)
C_ℓ +Minkowski(LOG)	9275 (+136%)	0.906 (+17%)	0.726 (+42%)	5.41 (+44%)	0.85 (+9%)
C_ℓ + ℓ_1 -norm(LOG)	6740 (+71%)	0.81 (+26%)	0.947 (+25%)	6.95 (+28%)	1.05 (-12%)
C_ℓ +Peaks(LOG) +Voids(LOG)	11446 (+191%)	0.824 (+24%)	0.658 (+48%)	4.81 (+50%)	0.66 (+29%)
C_ℓ +Minkowski(LOG) + ℓ_1 -norm(LOG)	9571 (+144%)	0.893 (+18%)	0.681 (+46%)	4.95 (+49%)	0.722 (+23%)
C_ℓ +Peaks(LOG) +Minkowski(LOG)	13285 (+238%)	0.679 (+38%)	0.648 (+48%)	4.89 (+50%)	0.683 (+27%)
C_ℓ +Voids(LOG) +Minkowski(LOG)	11319 (+188%)	0.76 (+30%)	0.626 (+50%)	5.08 (+48%)	0.574 (+38%)
C_ℓ +Peaks(LOG) +Voids(LOG) +Minkowski(LOG) + ℓ_1 -norm(LOG)	16431 (+319%)	0.654 (+40%)	0.588 (+53%)	4.47 (+54%)	0.559 (+40%)

similarity of the ℓ_1 -norm and the V_0 Minkowski functional (compare Equations 2.26 and 2.27).

Overall, the strongest constraints are found when combining the angular power spectrum with extrema statistics plus topological statistics. While the best constraints are observed when combining all the summary statistics, it seems that the combination of the angular power spectrum with the peak counts and the Minkowski functionals is the most ‘cost-effective’ one, given that it only includes three statistics, but at the same time achieves a very high precision.

It is worth noticing that most of these combinations of statistics significantly outperform the angular power spectrum, even in the case when all scales up to $\ell = 2048$ are considered in the angular power spectrum only case. Hence, our results indicate that the findings of Z21a, who showed that the addition of higher order statistics can compensate for the information loss caused by stringent scale cuts due to baryonic physics, are also valid at the stage 4 survey level and when considering the full w CDM parameter space.

We note that, while the constraints on the remaining w CDM parameters (n_s , Ω_b and H_0) are prior dominated in our analysis using the individual statistics, the combined statistics approach allows to put some non-prior-dominated constraints on these parameters (see Figure 10 in Appendix B).

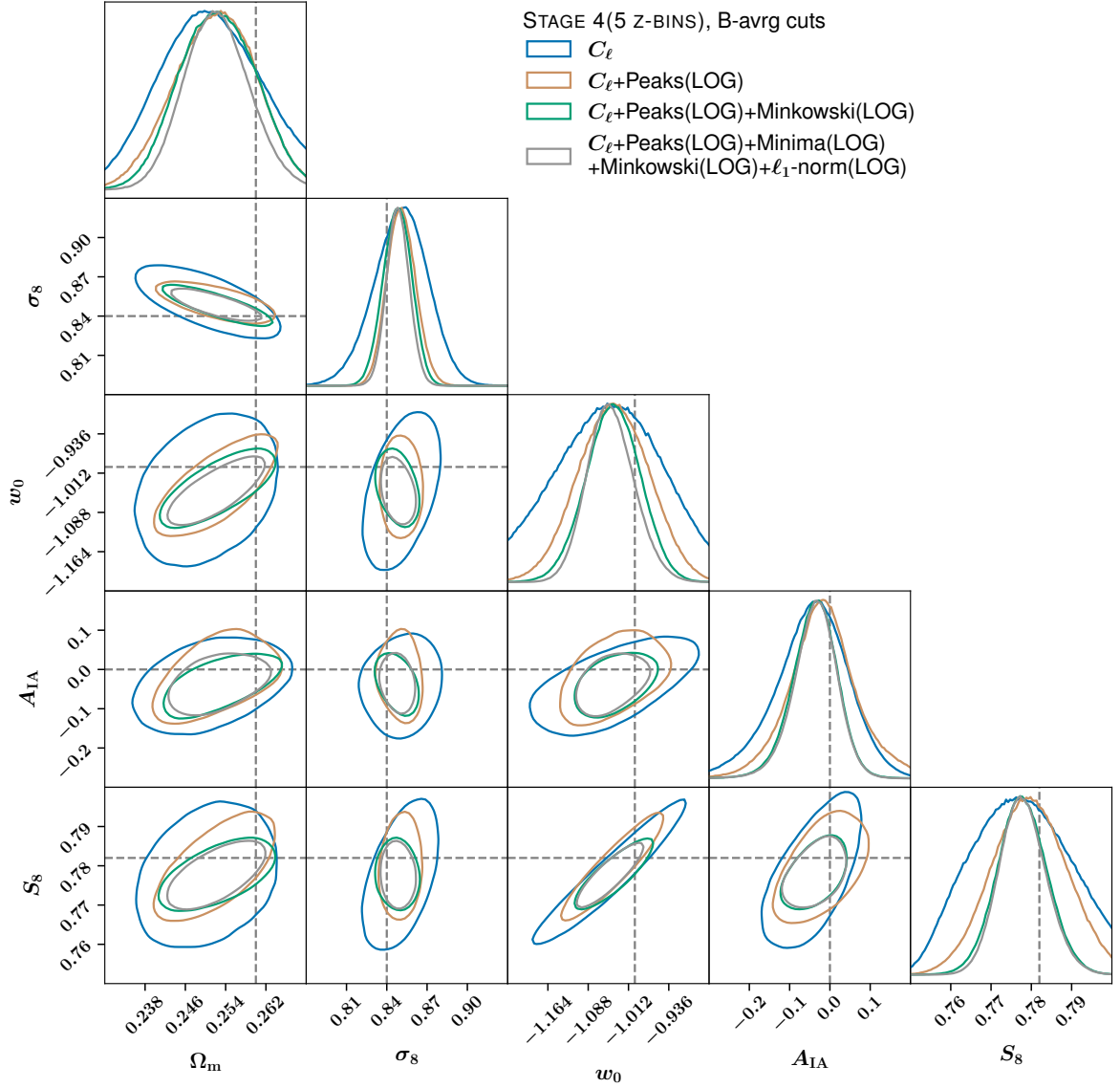


Figure 7. Fiducial constraints on Ω_m , σ_8 , w_0 and S_8 as well as A_{IA} for a selection of the combined summary statistics. The presented constraints are derived for the STAGE 4 (5 z-BINS) survey setup using the most favourable filter scheme for the higher order statistics (namely the LOG scheme). The best-guess model B-avg scale cuts are applied (see Table 4). The contours show the 68% confidence regions. The dashed grey lines are located at the true parameter values.

6 Conclusions

The ongoing stage 3 and upcoming stage 4 weak lensing surveys will allow us to map of the matter distribution in the local Universe with exceptional precision and thus provide a wealth of cosmological information. To fully utilize this information for cosmological parameter inference, the use of higher order mass map statistics in addition to the more commonly used two-point statistics is essential (see [134] for example). However, with the increased precision of such surveys, new theoretical as well as computational challenges arise for the analyses of such surveys.

In this work, we further improve the framework initially introduced in Z21a and successfully applied to the Dark Energy Survey Year 3 data by Z21b to match some of the requirements posed by stage 4 surveys. Most notably, this includes the extension of the probed parameter space to the full w CDM space.

Furthermore, we forecast the cosmological constraints that can be expected from such surveys, using the angular power spectrum, peak counts, minima counts, Minkowski functionals and the ℓ_1 -norm of the mass maps and we make suggestions for some analysis choices. Our main conclusions are as follows:

- We compare different filter schemes for the higher order mass map statistics and we find a consistent preference for Starlet based filters over Gaussian filters, yielding higher constraining power. We also find, that distributing the cut-off frequencies of the Starlet filters further apart in log space instead of the originally proposed dyadic spacing is more favourable for this kind of analysis. This can be attributed to the fact, that more of the filters are located at smaller scales, while the dyadic scheme focuses more on the large scales.
- A comparison of the cosmological constraining power of the different summary statistics between a stage 4 survey setup with 5 and 10 tomographic bins revealed that all studied statistics profit from the increase in tomographic resolution.
- We find the peak counts and the angular power spectrum to provide the most stringent constraints on the cosmological parameters in all tested setups. For the higher order mass map statistics peak counts achieve the highest precision, closely followed by minima counts. The extrema statistics outperform the Minkowski functionals and the ℓ_1 -norm that are both geared more towards capturing the global topology of the mass maps. The Minkowski functionals are found to outperform the ℓ_1 -norm in all setups.
- We find all constraints to improve greatly if galaxy intrinsic alignment is not considered in the analysis. None of the statistics show significant robustness against galaxy intrinsic alignment for stage 4 surveys. The angular power spectrum is found to constrain the galaxy intrinsic alignment amplitude A_{IA} the strongest.
- Removing the cross-tomographic bins (1x2, 1x3, etc.) from the analysis, causes the galaxy intrinsic alignment constraints, and hence also the cosmological constraints, to weaken considerably. This holds true for all studied summary statistics. Hence, we conclude that all statistics profit significantly from the cross-tomographic information.
- We derive the necessary scale cuts that need to be applied in a stage 4 scenario for the summary statistics to stay unaffected by baryonic physics, that is not modelled in dark-matter-only simulations. Due to the increased constraining power of stage 4 surveys the scale cuts are more stringent than in a stage 3 scenario leading to a significant drop of the constraining power of all summary statistics.
- We find that combining multiple summary statistics has the potential to extract different, independent types of features and information from the mass maps. Combining different summary statistics is found to yield competitive constraints even when restricted by the conservative stage 4 scale cuts, enforced by unmodelled baryonic effects in the dark-matter-only simulations. Using such a combination of summary statistics provides an alternative, computationally more feasible way to obtain tight constraints

on the w CDM model, compared to modelling small scale baryonic physics in the simulations. Additionally, we find the combined approach to mildly constrain the parameters n_s , Ω_b , H_0 and η , which are prior-dominated in our analyses using the individual statistics.

While we extended the method originally proposed by Z21a to meet some of the requirements of a stage 4 survey analysis in this work, we note that there are further known and potentially also unknown systematic effects that might require additional scale cuts or modifications of the presented methodology. Firstly, the Born approximation used in `UFalcon` was shown to be inaccurate for higher order statistics in a stage 4 setting [94] and a full ray tracing algorithm should be used instead. Secondly, [135] have demonstrated that the covariance matrix varies significantly with cosmology. This effect has to be taken into account in a stage 4 scenario. A possible way to take the cosmology dependence in account was explored by [136] and is applicable to our methodology. We note, that the non-linear intrinsic alignment model (NLA) is approximate and does not take into account the tidal torque field. Instead, the treatment of galaxy intrinsic alignment should be extended to the tidal alignment and tidal torquing model (TATT) [137]. While we focused on forecasting constraints without a baryonic treatment in this study we further note that the procedure presented by [41] is applicable to our methodology and could be used to include baryonic effects into the analysis and to relax some of the scale cuts. The above listed issues will be addressed in future studies.

Acknowledgments

The ETH Zurich Cosmology group at the Institute for Particle Physics and Astrophysics acknowledges support by grant 200021_192243 from the Swiss National Science Foundation.

The COSMOGRID simulations were created as a part of the Swiss National Supercomputing Center (CSCS) Production Project “Measuring Dark Energy with Deep Learning”. We thank Aurel Schneider for the help with baryon feedback models.

Some of the results in this paper have been derived using the `healpy` and `HEALPix` packages.

In this study, we made use of the functionalities provided by `numpy` [138], `scipy` [139], `matplotlib` [140] `tensorflow` [114] and `scikit-learn` [111].

We thank the main developers of `CosmoStat` (Jean-Luc Starck, Samuel Farrens and François Lanusse) and `Sparse2D`¹⁷ (Samuel Farrens, François Lanusse, Jean-Luc Starck, Mosè Giodano and Antoine Grigis) for making the mentioned software packages publicly available.

We thank Antony Lewis for the distribution of `GetDist`, on which we relied to produce some of the plots presented in this work [141].

We would also like to thank Uwe Schmitt from ETH Zürich for his support with the GitLab server and CI engine.

¹⁷<http://www.cosmostat.org/software/isap>

Further, we would like to thank Jean-Luc Starck from CEA-Saclay for his valuable input regarding this project.

A Distribution of the used COSMOGRID simulations

We present the distribution of the 315 used COSMOGRID simulations in the sampled eight dimensional parameter space that is spanned by the six w CDM parameters (Ω_m , Ω_b , σ_8 , n_s , H_0 and w_0) and the two NLA model parameters (A_{IA} and η). Each point in the parameter space is sampled by seven fully-independent PKDGRAV3 simulations.

B Fiducial constraints on full w CDM parameter space

We include a visualisation of the constraints on the full w CDM parameter space as obtained from the fiducial analysis discussed in Section 5.7. The constraints for the individual summary statistics are shown in Figures 9, while the contours for a selection of the combined statistics are presented in Figures 10.

C Parameter constraints without scale cuts

We present a forecast for the constraints on the full w CDM parameter space. No scale cuts apart from the cuts mentioned at the beginning of Section 5 are applied. We present the derived uncertainties of the 1D-posterior distributions of the three most constrained w CDM parameters Ω_m , S_8 and w_0 as well as the Figure of Merit (FoM) of the multidimensional contours in Table 6. The FoM is calculated according to Equation 5.1 using the parameter space covariance matrix obtained from the MCMC chains. We report the uncertainties for all investigated summary statistics using the three different filter schemes (GAUSS, LOG and DYADIC) and the three survey setups (STAGE 3, STAGE 4 (5 Z-BINS) and STAGE 4 (10 Z-BINS)).

References

- [1] D. Zürcher, J. Fluri, R. Sgier, T. Kacprzak and A. Refregier, *Cosmological forecast for non-gaussian statistics in large-scale weak lensing surveys*, *Journal of Cosmology and Astroparticle Physics* **2021** (2021) 028.
- [2] M. Bartelmann and P. Schneider, *Weak gravitational lensing*, *Physics Reports* **340** (Jan., 2001) 291–472, [[astro-ph/9912508](#)].
- [3] P. Schneider, *Weak gravitational lensing*, in *Gravitational lensing: strong, weak and micro*, pp. 269–451. Springer, 2006.
- [4] M. Kilbinger, *Cosmology with cosmic shear observations: a review*, *Reports on Progress in Physics* **78** (2015) 086901.
- [5] C. Heymans, E. Grocutt, A. Heavens, M. Kilbinger, T. D. Kitching, F. Simpson et al., *Cfhtlens tomographic weak lensing cosmological parameter constraints: Mitigating the impact of intrinsic galaxy alignments*, *Monthly Notices of the Royal Astronomical Society* **432** (2013) 2433–2453.

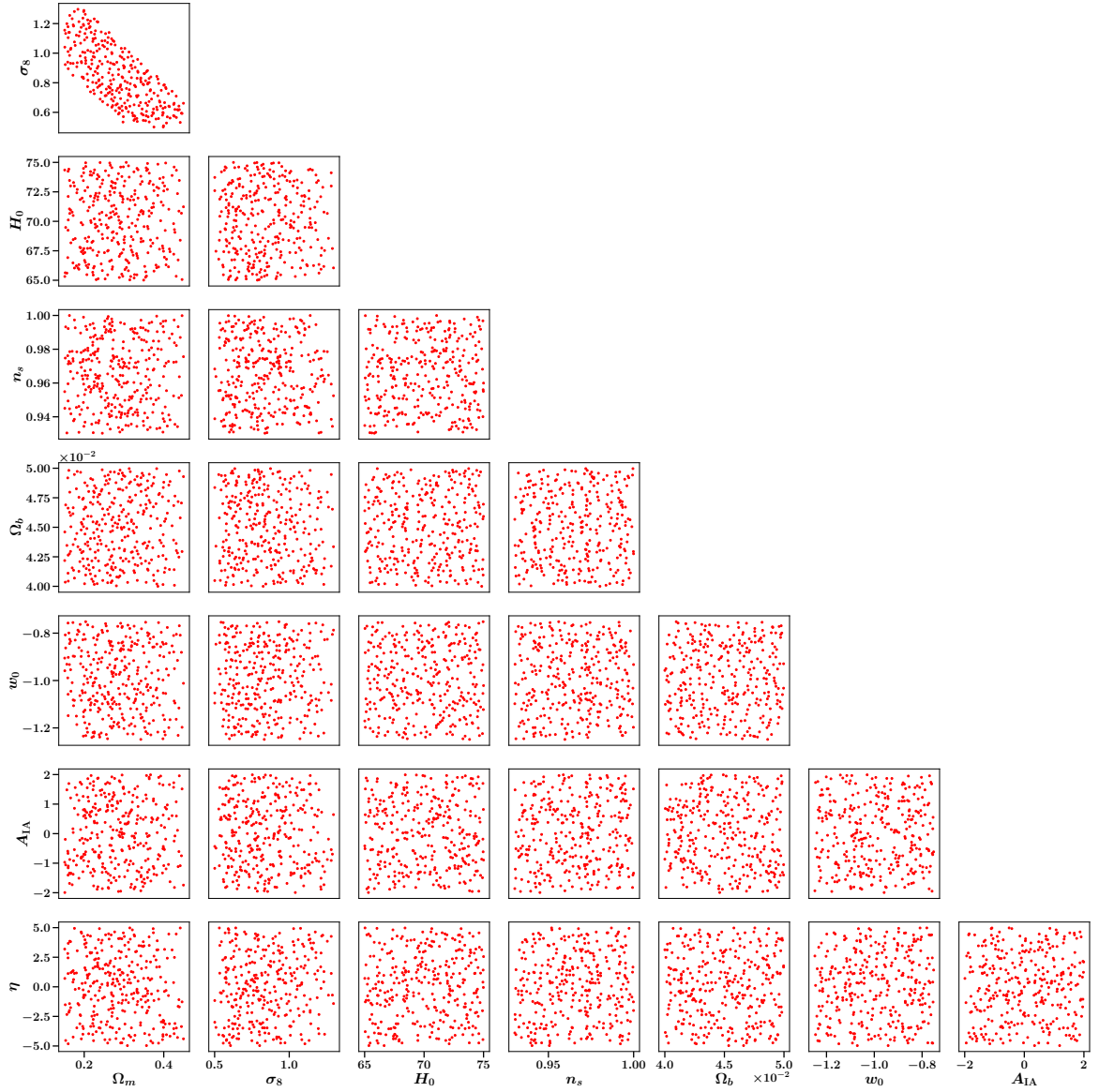


Figure 8. Distribution of the used COSMOGRID simulations in the full parameter space spanned by the six w CDM parameters (Ω_m , Ω_b , σ_8 , n_s , H_0 and w_0) and the two NLA model parameters (A_{IA} and η).

- [6] H. Hildebrandt, F. Köhlinger, J. Van den Busch, B. Joachimi, C. Heymans, A. Kannawadi et al., *Kids+ viking-450: Cosmic shear tomography with optical and infrared data*, *Astronomy & Astrophysics* **633** (2020) A69.
- [7] M. Asgari, C.-A. Lin, B. Joachimi, B. Giblin, C. Heymans, H. Hildebrandt et al., *Kids-1000 cosmology: Cosmic shear constraints and comparison between two point statistics*, *Astronomy & Astrophysics* **645** (2021) A104.
- [8] C. Hikage, M. Oguri, T. Hamana, S. More, R. Mandelbaum, M. Takada et al., *Cosmology from cosmic shear power spectra with subaru hyper supprime-cam first-year data*, *Publications of the Astronomical Society of Japan* **71** (2019) 43.
- [9] M. A. Troxel, N. MacCrann, J. Zuntz, T. Eifler, E. Krause, S. Dodelson et al., *Dark energy*

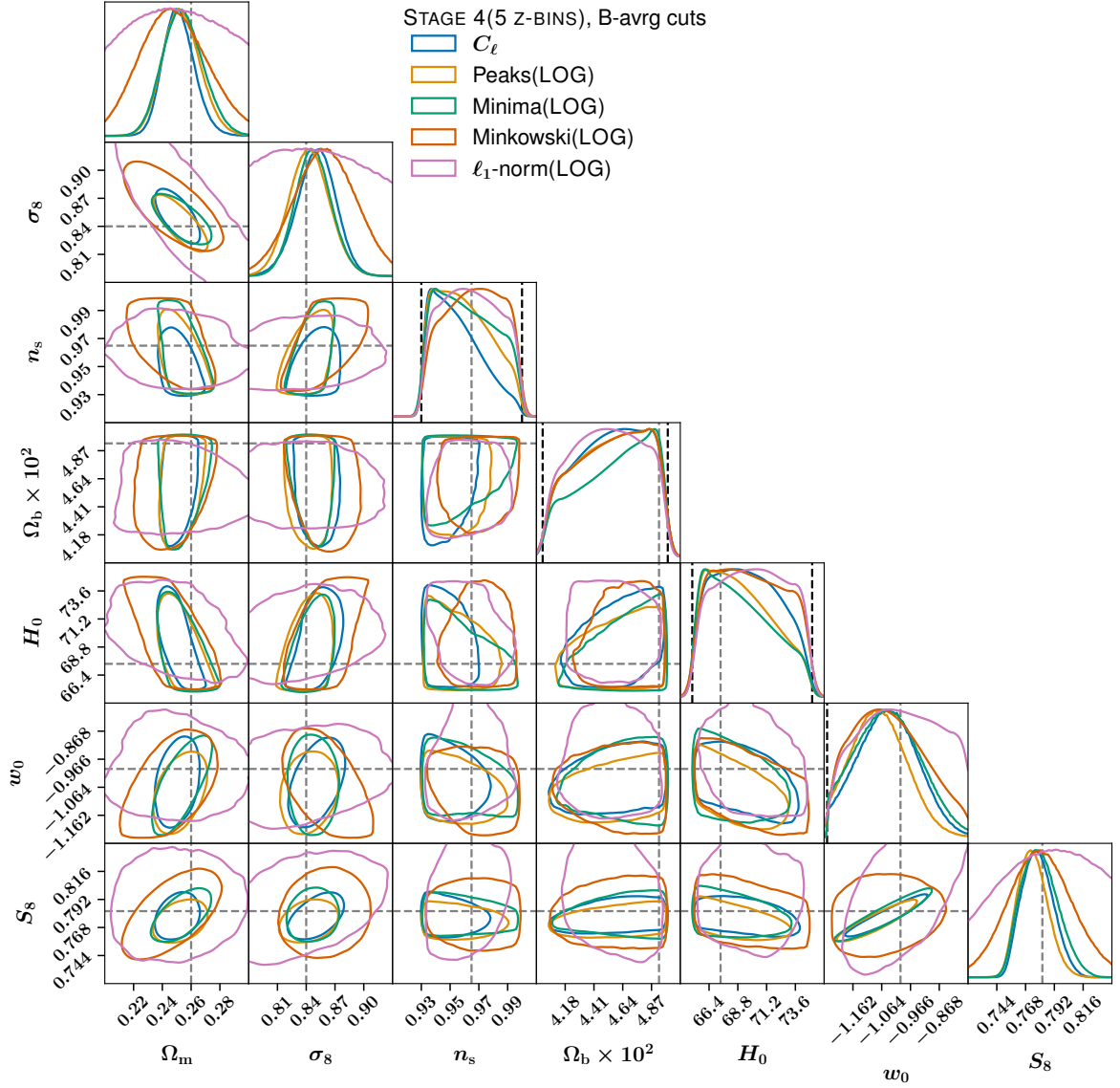


Figure 9. Fiducial constraints on the full w CDM parameter space as found in the STAGE 4 (5 Z-BINS) survey setup using the most favourable filter scheme for the higher order statistics (namely the LOG scheme). The B-avrg model scale cuts are used in this analysis. The contours show the 68% confidence regions. The dashed grey lines are located at the true parameter values. We indicate the prior boundaries using a black dashed line in the panels showing the 1D constraints, if the constraints are restricted by the prior.

survey year 1 results: Cosmological constraints from cosmic shear, Physical Review D **98** (2018) 043528.

- [10] L. Secco, S. Samuroff, E. Krause, B. Jain, J. Blazek, M. Raveri et al., *Dark energy survey year 3 results: Cosmology from cosmic shear and robustness to modeling uncertainty, Physical Review D* **105** (2022) 023515.
- [11] A. Amon, D. Gruen, M. Troxel, N. MacCrann, S. Dodelson, A. Choi et al., *Dark energy survey year 3 results: Cosmology from cosmic shear and robustness to data calibration, Physical Review D* **105** (2022) 023514.

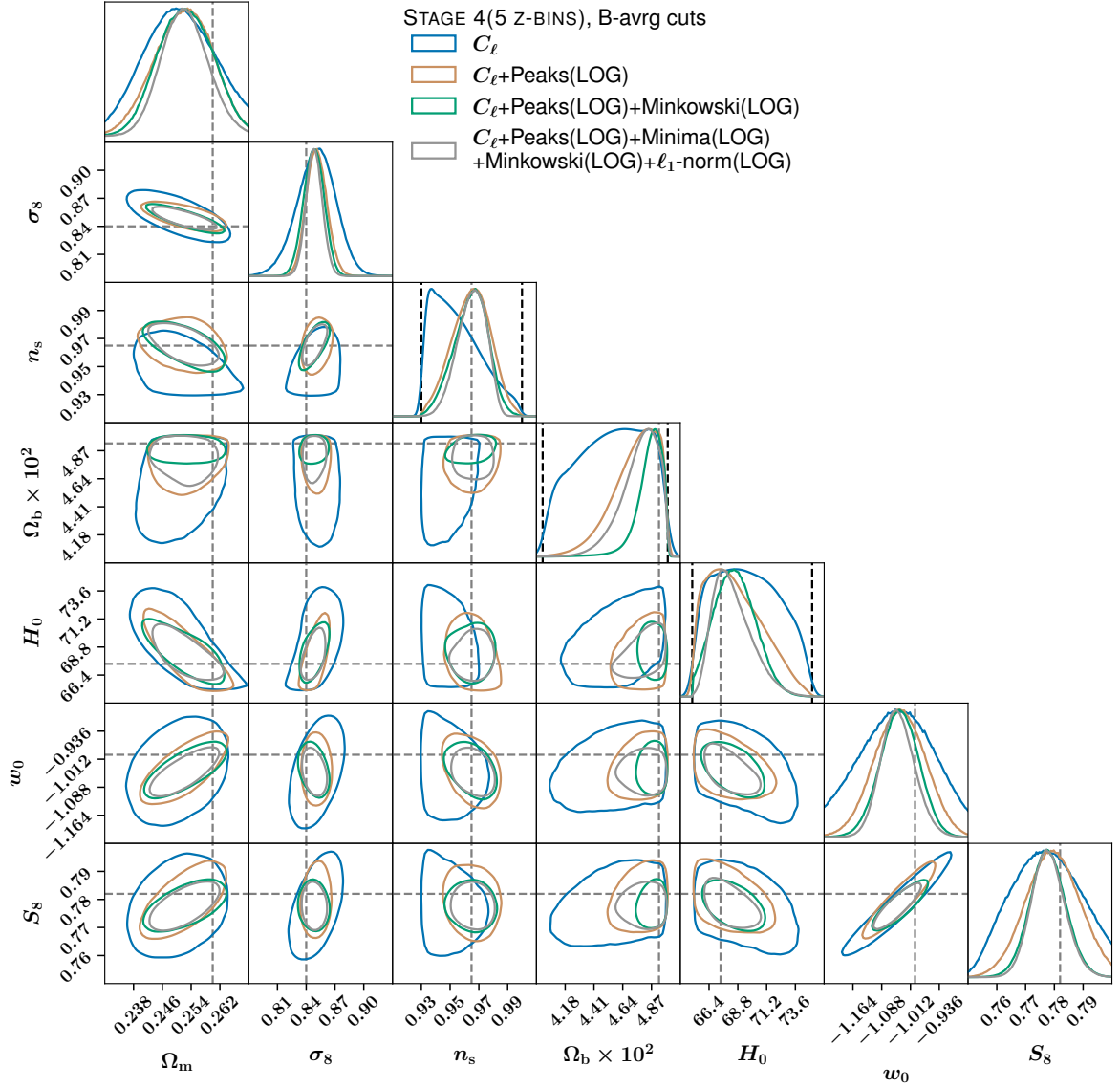


Figure 10. Fiducial constraints on the full w CDM parameter space as found in the STAGE 4 (5 z-BINS) survey setup for a selection of the combined statistics. The B-avrg model scale cuts are used in this analysis. The contours show the 68% confidence regions. The dashed grey lines are located at the true parameter values. We indicate the prior boundaries using a black dashed line in the panels showing the 1D constraints, if the constraints are restricted by the prior.

- [12] C. Chang, M. Jarvis, B. Jain, S. Kahn, D. Kirkby, A. Connolly et al., *The effective number density of galaxies for weak lensing measurements in the lsst project*, *Monthly Notices of the Royal Astronomical Society* **434** (2013) 2121–2135.
- [13] D. Spergel, N. Gehrels, C. Baltay, D. Bennett, J. Breckinridge, M. Donahue et al., *Wide-field infrared survey telescope-astronomy focused telescope assets wfirst-afta 2015 report*, *arXiv preprint arXiv:1503.03757* (2015) .
- [14] R. Laureijs, J. Amiaux, S. Arduini, J.-L. Augeres, J. Brinchmann, R. Cole et al., *Euclid definition study report*, *arXiv preprint arXiv:1110.3193* (2011) .

Table 6. We present the uncertainties of the 1D-posterior distributions of the three most constrained w CDM parameters Ω_m, S_8 and w_0 as well as the Figure of Merit (FoM). The uncertainties are reported as the standard deviations of the 1D posteriors. Additionally, we report on the relative change of the higher order statistics over the angular power spectrum constraints for each survey setup. No scale cuts were applied. We include the relative change of the values in comparison to the angular power spectrum results for each survey setup in brackets.

Statistic	$FoM(\Omega_m, S_8, w_0)$	$\sigma(\Omega_m) \times 10^2$	$\sigma(S_8) \times 10^2$	$\sigma(w_0) \times 10^2$
STAGE 3, all scales				
C_ℓ	3471 (-)	1.37 (-)	0.966 (-)	9.16 (-)
Peaks (GAUSS)	3183 (-8%)	1.51 (-10%)	1.09 (-12%)	8.96 (+2%)
Minima (GAUSS)	2833 (-18%)	1.68 (-23%)	1.08 (-11%)	8.91 (+2%)
Minkowski (GAUSS)	594 (-82%)	3.4 (-148%)	2.63 (-172%)	12.1 (-32%)
Peaks (LOG)	4231 (+21%)	1.43 (-4%)	1.08 (-11%)	9.0 (+1%)
Minima (LOG)	2910 (-16%)	1.67 (-22%)	1.06 (-9%)	9.01 (+1%)
Minkowski (LOG)	691 (-80%)	3.43 (-150%)	2.43 (-151%)	11.4 (-24%)
ℓ_1 -norm (LOG)	687 (-80%)	2.36 (-72%)	2.72 (-181%)	12.1 (-31%)
Peaks (DYADIC)	904 (-73%)	2.0 (-45%)	2.34 (-142%)	11.7 (-27%)
Minima (DYADIC)	756 (-78%)	2.43 (-77%)	2.35 (-143%)	12.6 (-37%)
Minkowski (DYADIC)	455 (-86%)	3.3 (-141%)	3.51 (-262%)	9.41 (-2%)
ℓ_1 -norm (DYADIC)	643 (-81%)	3.13 (-128%)	2.16 (-123%)	10.4 (-13%)
STAGE 4 (5 Z-BINS), all scales				
C_ℓ	8413 (-)	0.871 (-)	0.69 (-)	6.57 (-)
Peaks (GAUSS)	7502 (-10%)	1.08 (-23%)	0.777 (-12%)	6.6 (0%)
Minima (GAUSS)	7047 (-16%)	1.27 (-45%)	0.875 (-26%)	7.49 (-13%)
Minkowski (GAUSS)	1537 (-81%)	1.98 (-127%)	1.47 (-112%)	8.5 (-29%)
Peaks (LOG)	8936 (+6%)	1.15 (-32%)	0.747 (-8%)	6.35 (+3%)
Minima (LOG)	8195 (-2%)	1.1 (-26%)	0.731 (-5%)	6.1 (+7%)
Minkowski (LOG)	2347 (-72%)	1.39 (-59%)	2.11 (-206%)	3.58 (+45%)
ℓ_1 -norm (LOG)	744 (-91%)	2.34 (-168%)	2.54 (-268%)	11.7 (-78%)
Peaks (DYADIC)	1589 (-81%)	1.49 (-70%)	1.76 (-154%)	10.3 (-57%)
Minima (DYADIC)	1541 (-81%)	1.61 (-84%)	1.53 (-122%)	10.2 (-55%)
Minkowski (DYADIC)	1424 (-83%)	2.03 (-133%)	1.47 (-113%)	11.0 (-67%)
ℓ_1 -norm (DYADIC)	718 (-91%)	2.82 (-224%)	2.23 (-222%)	10.2 (-55%)
STAGE 4 (10 Z-BINS), all scales				
C_ℓ	10985 (-)	0.905 (-)	0.681 (-)	7.01 (-)
Peaks (GAUSS)	9132 (-16%)	0.964 (-6%)	0.586 (+13%)	5.38 (+23%)
Minima (GAUSS)	9659 (-12%)	1.06 (-17%)	0.678 (0%)	6.2 (+11%)
Minkowski (GAUSS)	2102 (-80%)	1.78 (-97%)	1.3 (-90%)	6.86 (+2%)
Peaks (LOG)	10063 (-8%)	0.901 (0%)	0.671 (+1%)	5.61 (+19%)
Minima (LOG)	9969 (-9%)	1.0 (-10%)	0.633 (+7%)	6.25 (+10%)
Minkowski (LOG)	5462 (-50%)	1.09 (-20%)	1.34 (-97%)	1.91 (+72%)
ℓ_1 -norm (LOG)	1657 (-84%)	1.88 (-107%)	1.56 (-128%)	6.83 (+2%)
Peaks (DYADIC)	1804 (-83%)	1.52 (-68%)	1.55 (-127%)	8.5 (-21%)
Minima (DYADIC)	2088 (-80%)	1.18 (-30%)	1.57 (-129%)	7.5 (-6%)
Minkowski (DYADIC)	1898 (-82%)	1.68 (-86%)	1.31 (-92%)	7.96 (-13%)
ℓ_1 -norm (DYADIC)	1049 (-90%)	1.78 (-97%)	2.33 (-242%)	10.4 (-48%)

[15] L. F. Secco, S. Samuroff, E. Krause, B. Jain, J. Blazek, M. Raveri et al., *Dark Energy Survey Year 3 Results: Cosmology from Cosmic Shear and Robustness to Modeling Uncertainty*,

arXiv e-prints (May, 2021) arXiv:2105.13544, [[2105.13544](#)].

- [16] V. Springel, C. S. Frenk and S. D. M. White, *The large-scale structure of the Universe*, *Nature* **440** (Apr., 2006) 1137–1144, [[astro-ph/0604561](#)].
- [17] X. Yang, J. M. Kratochvil, S. Wang, E. A. Lim, Z. Haiman and M. May, *Cosmological information in weak lensing peaks*, *Physical Review D* **84** (Aug., 2011) 043529, [[1109.6333](#)].
- [18] M. Takada and B. Jain, *The three-point correlation function in cosmology*, *Monthly Notices of the Royal Astronomical Society* **340** (Apr., 2003) 580–608, [[astro-ph/0209167](#)].
- [19] E. Semboloni, T. Schrabback, L. van Waerbeke, S. Vafaei, J. Hartlap and S. Hilbert, *Weak lensing from space: first cosmological constraints from three-point shear statistics*, *Monthly Notices of the Royal Astronomical Society* **410** (Jan., 2011) 143–160, [[1005.4941](#)].
- [20] L. Fu, M. Kilbinger, T. Erben, C. Heymans, H. Hildebrandt, H. Hoekstra et al., *CFHTLenS: cosmological constraints from a combination of cosmic shear two-point and three-point correlations*, *Monthly Notices of the Royal Astronomical Society* **441** (July, 2014) 2725–2743, [[1404.5469](#)].
- [21] L. Van Waerbeke, J. Benjamin, T. Erben, C. Heymans, H. Hildebrandt, H. Hoekstra et al., *Cfhtlens: mapping the large-scale structure with gravitational lensing*, *Monthly Notices of the Royal Astronomical Society* **433** (2013) 3373–3388.
- [22] K. Patton, J. Blazek, K. Honscheid, E. Huff, P. Melchior, A. J. Ross et al., *Cosmological constraints from the convergence 1-point probability distribution*, *Monthly Notices of the Royal Astronomical Society* **472** (Nov., 2017) 439–446, [[1611.01486](#)].
- [23] M. Gatti, C. Chang, O. Friedrich, B. Jain, D. Bacon, M. Crocce et al., *Dark Energy Survey Year 3 results: cosmology with moments of weak lensing mass maps - validation on simulations*, *Monthly Notices of the Royal Astronomical Society* **498** (Nov., 2020) 4060–4087, [[1911.05568](#)].
- [24] M. Gatti, B. Jain, C. Chang, M. Raveri, D. Zürcher, L. Secco et al., *Dark energy survey year 3 results: cosmology with moments of weak lensing mass maps*, *arXiv preprint arXiv:2110.10141* (2021) .
- [25] M. Shirasaki and N. Yoshida, *Statistical and Systematic Errors in the Measurement of Weak-Lensing Minkowski Functionals: Application to the Canada-France-Hawaii Lensing Survey*, *The Astrophysical Journal* **786** (May, 2014) 43, [[1312.5032](#)].
- [26] A. Petri, J. Liu, Z. Haiman, M. May, L. Hui and J. M. Kratochvil, *Emulating the CFHTLenS weak lensing data: Cosmological constraints from moments and Minkowski functionals*, *Physical Review D* **91** (May, 2015) 103511, [[1503.06214](#)].
- [27] C. Parroni, V. F. Cardone, R. Maoli and R. Scaramella, *Going deep with Minkowski functionals of convergence maps*, *Astronomy & Astrophysics* **633** (Jan., 2020) A71, [[1911.06243](#)].
- [28] B. Jain and L. Van Waerbeke, *Statistics of dark matter halos from gravitational lensing*, *The Astrophysical Journal Letters* **530** (2000) L1.
- [29] J. P. Dietrich and J. Hartlap, *Cosmology with the shear-peak statistics*, *Monthly Notices of the Royal Astronomical Society* **402** (Feb., 2010) 1049–1058, [[0906.3512](#)].
- [30] H. Shan, X. Liu, H. Hildebrandt, C. Pan, N. Martinet, Z. Fan et al., *KiDS-450: cosmological constraints from weak lensing peak statistics - I. Inference from analytical prediction of high signal-to-noise ratio convergence peaks*, *Monthly Notices of the Royal Astronomical Society* **474** (Feb., 2018) 1116–1134, [[1709.07651](#)].
- [31] J. Fluri, T. Kacprzak, R. Sgier, A. Refregier and A. Amara, *Weak lensing peak statistics in the era of large scale cosmological surveys*, *Journal of Cosmology and Astroparticle Physics* **2018** (2018) 051.

- [32] N. Martinet, P. Schneider, H. Hildebrandt, H. Shan, M. Asgari, J. P. Dietrich et al., *KiDS-450: cosmological constraints from weak-lensing peak statistics - II: Inference from shear peaks using N-body simulations*, *Monthly Notices of the Royal Astronomical Society* **474** (Feb., 2018) 712–730, [[1709.07678](#)].
- [33] J. Harnois-Déraps, N. Martinet, T. Castro, K. Dolag, B. Giblin, C. Heymans et al., *Cosmic shear cosmology beyond 2-point statistics: A combined peak count and correlation function analysis of des-y1*, *arXiv preprint arXiv:2012.02777* (2020) .
- [34] N. Jeffrey, J. Alsing and F. Lanusse, *Likelihood-free inference with neural compression of DES SV weak lensing map statistics*, *Monthly Notices of the Royal Astronomical Society* **501** (Feb., 2021) 954–969, [[2009.08459](#)].
- [35] T. Kacprzak, D. Kirk, O. Friedrich, A. Amara, A. Refregier, L. Marian et al., *Cosmology constraints from shear peak statistics in dark energy survey science verification data*, *Monthly Notices of the Royal Astronomical Society* **463** (2016) 3653–3673.
- [36] W. R. Coulton, J. Liu, I. G. McCarthy and K. Osato, *Weak lensing minima and peaks: Cosmological constraints and the impact of baryons*, *Monthly Notices of the Royal Astronomical Society* **495** (2020) 2531–2542.
- [37] V. Ajani, J.-L. Starck and V. Pettorino, *Starlet ℓ_1 -norm for weak lensing cosmology*, *Astronomy & Astrophysics* **645** (2021) L11.
- [38] E. Allys, T. Marchand, J.-F. Cardoso, F. Villaescusa-Navarro, S. Ho and S. Mallat, *New interpretable statistics for large-scale structure analysis and generation*, *Physical Review D* **102** (2020) 103506.
- [39] A. Gupta, J. M. Zorrilla Matilla, D. Hsu and Z. Haiman, *Non-Gaussian information from weak lensing data via deep learning*, *Physical Review D* **97** (May, 2018) 103515, [[1802.01212](#)].
- [40] J. Fluri, T. Kacprzak, A. Lucchi, A. Refregier, A. Amara, T. Hofmann et al., *Cosmological constraints with deep learning from KiDS-450 weak lensing maps*, *Physical Review D* **100** (Sept., 2019) 063514, [[1906.03156](#)].
- [41] J. Fluri, T. Kacprzak, A. Lucchi, A. Schneider, A. Refregier and T. Hofmann, *A full w Λ CDM analysis of kids-1000 weak lensing maps using deep learning*, *arXiv preprint arXiv:2201.07771* (2022) .
- [42] M. Gatti, E. Sheldon, A. Amon, M. Becker, M. Troxel, A. Choi et al., *Dark energy survey year 3 results: Weak lensing shape catalogue*, *arXiv preprint arXiv:2011.03408* (2020) .
- [43] D. Zürcher, J. Fluri, R. Sgier, T. Kacprzak, M. Gatti, C. Doux et al., *Dark energy survey year 3 results: Cosmology with peaks using an emulator approach*, *arXiv preprint arXiv:2110.10135* (2021) .
- [44] T. Kacprzak, J. Fluri, A. Schneider, A. Refregier, J. Stadel et al., *COSMOGRID: a fully numerical w CDM theory prediction for large scale structure cosmology*, *To be submitted to Journal of Cosmology and Astroparticle Physics* (2022) .
- [45] J.-L. Starck, J. Fadili and F. Murtagh, *The undecimated wavelet decomposition and its reconstruction*, *IEEE transactions on image processing* **16** (2007) 297–309.
- [46] N. Jeffrey, M. Gatti, C. Chang, L. Whiteway, U. Demirbozan, A. Kovacs et al., *Dark energy survey year 3 results: Curved-sky weak lensing mass map reconstruction*, *Monthly Notices of the Royal Astronomical Society* **505** (2021) 4626–4645.
- [47] N. Kaiser, G. Squires and T. Broadhurst, *A method for weak lensing observations*, *arXiv preprint astro-ph/9411005* (1994) .
- [48] C. G. Wallis, M. A. Price, J. D. McEwen, T. D. Kitching, B. Leistedt and A. Plouviez, *Mapping dark matter on the celestial sphere with weak gravitational lensing*, *Monthly Notices of the Royal Astronomical Society* (2017) .

- [49] K. M. Gorski, E. Hivon, A. J. Banday, B. D. Wandelt, F. K. Hansen, M. Reinecke et al., *Healpix: A framework for high-resolution discretization and fast analysis of data distributed on the sphere*, *The Astrophysical Journal* **622** (2005) 759.
- [50] D. N. Limber, *The analysis of counts of the extragalactic nebulae in terms of a fluctuating density field.*, *The Astrophysical Journal* **117** (1953) 134.
- [51] H. Hildebrandt, M. Viola, C. Heymans, S. Joudaki, K. Kuijken, C. Blake et al., *Kids-450: Cosmological parameter constraints from tomographic weak gravitational lensing*, *Monthly Notices of the Royal Astronomical Society* **465** (2017) 1454–1498.
- [52] C. Heymans, T. Tröster, M. Asgari, C. Blake, H. Hildebrandt, B. Joachimi et al., *KiDS-1000 Cosmology: Multi-probe weak gravitational lensing and spectroscopic galaxy clustering constraints*, *Astronomy & Astrophysics* **646** (Feb., 2021) A140, [[2007.15632](#)].
- [53] A. Amon, D. Gruen, M. A. Troxel, N. MacCrann, S. Dodelson, A. Choi et al., *Dark Energy Survey Year 3 Results: Cosmology from Cosmic Shear and Robustness to Data Calibration*, *arXiv e-prints* (May, 2021) arXiv:2105.13543, [[2105.13543](#)].
- [54] A. Zonca, L. P. Singer, D. Lenz, M. Reinecke, C. Rosset, E. Hivon et al., *healpy: equal area pixelization and spherical harmonics transforms for data on the sphere in python*, *Journal of Open Source Software* **4** (2019) 1298.
- [55] V. Ajani, A. Peel, V. Pettorino, J.-L. Starck, Z. Li and J. Liu, *Constraining neutrino masses with weak-lensing multiscale peak counts*, *Physical Review D* **102** (2020) 103531.
- [56] J.-L. Starck, Y. Moudden, P. Abrial and M. Nguyen, *Wavelets, ridgelets and curvelets on the sphere*, *Astronomy & Astrophysics* **446** (2006) 1191–1204.
- [57] J.-L. Starck, E. Pantin and F. Murtagh, *Deconvolution in astronomy: A review*, *Publications of the Astronomical Society of the Pacific* **114** (2002) 1051.
- [58] N. Aghanim and O. Forni, *Searching for the non-gaussian signature of the cmb secondary anisotropies*, *arXiv preprint astro-ph/9905124* (1999) .
- [59] R. B. Barreiro and M. Hobson, *The discriminating power of wavelets to detect non-gaussianity in the cosmic microwave background*, *Monthly Notices of the Royal Astronomical Society* **327** (2001) 813–828.
- [60] P. Vielva, E. Martínez-González, R. Barreiro, J. Sanz and L. Cayón, *Detection of non-gaussianity in the wilkinson microwave anisotropy probe first-year data using spherical wavelets*, *The Astrophysical Journal* **609** (2004) 22.
- [61] J.-L. Starck, N. Aghanim and O. Forni, *Detection and discrimination of cosmological non-gaussian signatures by multi-scale methods*, *Astronomy & Astrophysics* **416** (2004) 9–17.
- [62] L.-Z. Fang and L.-l. Feng, *Measuring the galaxy power spectrum and scale-scale correlations with multiresolution-decomposed covariance. i. method*, *The Astrophysical Journal* **539** (2000) 5.
- [63] J.-L. Starck, S. Pires and A. Réfrégier, *Weak lensing mass reconstruction using wavelets*, *Astronomy & Astrophysics* **451** (2006) 1139–1150.
- [64] F. Lanusse, *Reconstruction parcimonieuse de la carte de masse de matière noire par effet de lentille gravitationnelle*, Ph.D. thesis, 2015.
- [65] Lanusse, F., Starck, J.-L., Leonard, A. and Pires, S., *High resolution weak lensing mass mapping combining shear and flexion*, *A&A* **591** (2016) A2.
- [66] A. Peel, F. Lanusse and J.-L. Starck, *Sparse reconstruction of the merging a520 cluster system*, *The Astrophysical Journal* **847** (sep, 2017) 23.
- [67] J. Starck, F. Murtagh and J. Fadili, *Sparse Image and Signal Processing: Wavelets and Related Geometric Multiscale Analysis*. Cambridge University Press, 2015.

- [68] M. Holschneider, R. Kronland-Martinet, J. Morlet and P. Tchamitchian, *A real-time algorithm for signal analysis with the help of the wavelet transform*, in *Wavelets* (J.-M. Combes, A. Grossmann and P. Tchamitchian, eds.), (Berlin, Heidelberg), pp. 286–297, Springer Berlin Heidelberg, 1989.
- [69] J.-L. Starck, K. Themelis, N. Jeffrey, A. Peel and F. Lanusse, *Weak lensing mass reconstruction using sparsity and a gaussian random field*, *arXiv preprint arXiv:2102.04127* (2021) .
- [70] J.-L. Starck, F. Murtagh and J. M. Fadili, *Sparse image and signal processing: wavelets, curvelets, morphological diversity*. Cambridge university press, 2010.
- [71] K. Reblinsky, G. Kruse, B. Jain and P. Schneider, *Cosmic shear and halo abundances: analytical versus numerical results*, *arXiv preprint astro-ph/9907250* (1999) .
- [72] J. Liu and Z. Haiman, *Origin of weak lensing convergence peaks*, *Physical Review D* **94** (2016) 043533.
- [73] J. Harnois-Déraps, N. Martinet, T. Castro, K. Dolag, B. Giblin, C. Heymans et al., *Cosmic shear cosmology beyond two-point statistics: a combined peak count and correlation function analysis of des-y1*, *Monthly Notices of the Royal Astronomical Society* **506** (2021) 1623–1650.
- [74] J. A. Tyson, F. Valdes and R. Wenk, *Detection of systematic gravitational lens galaxy image alignments-mapping dark matter in galaxy clusters*, *The Astrophysical Journal* **349** (1990) L1–L4.
- [75] J. Miralda-Escude, *The correlation function of galaxy ellipticities produced by gravitational lensing*, *The Astrophysical Journal* **380** (1991) 1–8.
- [76] N. Kaiser and G. Squires, *Mapping the dark matter with weak gravitational lensing*, *The Astrophysical Journal* **404** (1993) 441–450.
- [77] P. Schneider, *Detection of (dark) matter concentrations via weak gravitational lensing*, *Monthly Notices of the Royal Astronomical Society* **283** (1996) 837–853.
- [78] T. Baker, J. Clampitt, B. Jain and M. Trodden, *Void lensing as a test of gravity*, *Physical Review D* **98** (2018) 023511.
- [79] E. Paillas, M. Cautun, B. Li, Y.-C. Cai, N. Padilla, J. Armijo et al., *The santiago-harvard-edinburgh-durham void comparison ii: unveiling the vainshtein screening using weak lensing*, *Monthly Notices of the Royal Astronomical Society* **484** (2019) 1149–1165.
- [80] A. Petri, Z. Haiman, L. Hui, M. May and J. M. Kratochvil, *Cosmology with minkowski functionals and moments of the weak lensing convergence field*, *Physical Review D* **88** (2013) 123002.
- [81] K. R. Mecke, T. Buchert and H. Wagner, *Robust morphological measures for large-scale structure in the universe*, *arXiv preprint astro-ph/9312028* (1993) .
- [82] M. Vicinanza, V. F. Cardone, R. Maoli, R. Scaramella, X. Er and I. Tereno, *Minkowski functionals of convergence maps and the lensing figure of merit*, *Physical Review D* **99** (2019) 043534.
- [83] D. E. S. Collaboration, *The dark energy survey*, *International Journal of Modern Physics A* **20** (2005) 3121–3123.
- [84] C. Bruderer, C. Chang, A. Refregier, A. Amara, J. Bergé and L. Gamper, *Calibrated ultra fast image simulations for the dark energy survey*, *The Astrophysical Journal* **817** (2016) 25.
- [85] I. Smail, D. W. Hogg, L. Yan and J. G. Cohen, *Deep optical galaxy counts with the keck telescope*, *The Astrophysical Journal Letters* **449** (1995) L105.
- [86] A. Amara and A. Réfrégier, *Optimal surveys for weak-lensing tomography*, *Monthly Notices of the Royal Astronomical Society* **381** (2007) 1018–1026.

- [87] R. Mandelbaum, T. Eifler, R. Hložek, T. Collett, E. Gawiser, D. Scolnic et al., *The lsst dark energy science collaboration (desc) science requirements document*, *arXiv preprint arXiv:1809.01669* (2018) .
- [88] T. Tram, J. Brandbyge, J. Dakin and S. Hannestad, *Fully relativistic treatment of light neutrinos in n-body simulations*, *Journal of Cosmology and Astroparticle Physics* **2019** (2019) 022.
- [89] D. Potter, J. Stadel and R. Teyssier, *Pkdgrav3: beyond trillion particle cosmological simulations for the next era of galaxy surveys*, *Computational Astrophysics and Cosmology* **4** (2017) 2.
- [90] J. Lesgourgues, *The Cosmic Linear Anisotropy Solving System (CLASS) I: Overview*, *arXiv e-prints* (Apr., 2011) arXiv:1104.2932, [[1104.2932](#)].
- [91] J. Dakin, J. Brandbyge, S. Hannestad, T. HaugbØlle and T. Tram, *ν CONCEPT: cosmological neutrino simulations from the non-linear Boltzmann hierarchy*, *Journal of Cosmology and Astroparticle Physics* **2019** (Feb., 2019) 052, [[1712.03944](#)].
- [92] E. Krause and T. Eifler, *cosmolike–cosmological likelihood analyses for photometric galaxy surveys*, *Monthly Notices of the Royal Astronomical Society* **470** (2017) 2100–2112.
- [93] R. J. Sgier, A. Réfrégier, A. Amara and A. Nicola, *Fast generation of covariance matrices for weak lensing*, *Journal of Cosmology and Astroparticle Physics* **2019** (2019) 044.
- [94] A. Petri, Z. Haiman and M. May, *Validity of the born approximation for beyond gaussian weak lensing observables*, *Physical Review D* **95** (2017) 123503.
- [95] Z. Li, J. Liu, J. M. Z. Matilla and W. R. Coulton, *Constraining neutrino mass with tomographic weak lensing peak counts*, *Physical Review D* **99** (2019) 063527.
- [96] M. Fong, M. Choi, V. Catlett, B. Lee, A. Peel, R. Bowyer et al., *The impact of baryonic physics and massive neutrinos on weak lensing peak statistics*, *Monthly Notices of the Royal Astronomical Society* **488** (2019) 3340–3357.
- [97] D. Huterer, M. Takada, G. Bernstein and B. Jain, *Systematic errors in future weak-lensing surveys: requirements and prospects for self-calibration*, *Monthly Notices of the Royal Astronomical Society* **366** (2006) 101–114.
- [98] A. Choi, C. Heymans, C. Blake, H. Hildebrandt, C. A. Duncan, T. Erben et al., *Cfhtlens and rslens: testing photometric redshift distributions using angular cross-correlations with spectroscopic galaxy surveys*, *Monthly Notices of the Royal Astronomical Society* **463** (2016) 3737–3754.
- [99] H. Hildebrandt, F. Köhlinger, J. van den Busch, B. Joachimi, C. Heymans, A. Kannawadi et al., *Kids+ viking-450: Cosmic shear tomography with optical and infrared data*, *Astronomy & Astrophysics* **633** (2020) A69.
- [100] S. Fischbacher, T. Kacprzak, J. Blazek and A. Refregier, “Calibration requirements for the width of redshift distribution for complex intrinsic alignment models.”.
- [101] C. M. Hirata, R. Mandelbaum, U. Seljak, J. Guzik, N. Padmanabhan, C. Blake et al., *Galaxy–galaxy weak lensing in the sloan digital sky survey: intrinsic alignments and shear calibration errors*, *Monthly Notices of the Royal Astronomical Society* **353** (2004) 529–549.
- [102] G. M. Bernstein, *Shape measurement biases from underfitting and ellipticity gradients*, *Monthly Notices of the Royal Astronomical Society* **406** (2010) 2793–2804.
- [103] A. Refregier, T. Kacprzak, A. Amara, S. Bridle and B. Rowe, *Noise bias in weak lensing shape measurements*, *Monthly Notices of the Royal Astronomical Society* **425** (2012) 1951–1957.
- [104] P. Melchior and M. Viola, *Means of confusion: how pixel noise affects shear estimates for*

- weak gravitational lensing*, *Monthly Notices of the Royal Astronomical Society* **424** (2012) 2757–2769.
- [105] L. Voigt and S. Bridle, *Limitations of model-fitting methods for lensing shear estimation*, *Monthly Notices of the Royal Astronomical Society* **404** (2010) 458–467.
 - [106] A. Heavens, A. Refregier and C. Heymans, *Intrinsic correlation of galaxy shapes: implications for weak lensing measurements*, *Monthly Notices of the Royal Astronomical Society* **319** (2000) 649–656.
 - [107] C. M. Hirata and U. Seljak, *Intrinsic alignment-lensing interference as a contaminant of cosmic shear*, *Physical Review D* **70** (2004) 063526.
 - [108] S. Bridle and L. King, *Dark energy constraints from cosmic shear power spectra: impact of intrinsic alignments on photometric redshift requirements*, *New Journal of Physics* **9** (2007) 444.
 - [109] B. Joachimi, R. Mandelbaum, F. Abdalla and S. Bridle, *Constraints on intrinsic alignment contamination of weak lensing surveys using the megaz-lrg sample*, *Astronomy & Astrophysics* **527** (2011) A26.
 - [110] K. Pearson, *Liii. on lines and planes of closest fit to systems of points in space*, *The London, Edinburgh, and Dublin philosophical magazine and journal of science* **2** (1901) 559–572.
 - [111] F. Pedregosa, G. Varoquaux, A. Gramfort, V. Michel, B. Thirion, O. Grisel et al., *Scikit-learn: Machine learning in Python*, *Journal of Machine Learning Research* **12** (2011) 2825–2830.
 - [112] D. Hendrycks and K. Gimpel, *Gaussian Error Linear Units (GELUs)*, *arXiv e-prints* (June, 2016) arXiv:1606.08415, [[1606.08415](#)].
 - [113] D. P. Kingma and J. Ba, *Adam: A method for stochastic optimization*, *arXiv preprint arXiv:1412.6980* (2014) .
 - [114] M. Abadi, A. Agarwal, P. Barham, E. Brevdo, Z. Chen, C. Citro et al., *TensorFlow: Large-scale machine learning on heterogeneous systems*, 2015.
 - [115] E. Sellentin and A. F. Heavens, *Parameter inference with estimated covariance matrices*, *Monthly Notices of the Royal Astronomical Society: Letters* **456** (2015) L132–L136.
 - [116] N. Jeffrey and F. B. Abdalla, *Parameter inference and model comparison using theoretical predictions from noisy simulations*, *Monthly Notices of the Royal Astronomical Society* **490** (2019) 5749–5756.
 - [117] F.-M. Daniel, D. W. Hogg, D. Lang and J. Goodman, *emcee: The mcmc hammer*, *Publications of the Astronomical Society of the Pacific* **125** (2013) 306.
 - [118] N. E. Chisari, D. Alonso, E. Krause, C. D. Leonard, P. Bull, J. Neveu et al., *Core cosmology library: Precision cosmological predictions for lsst*, *The Astrophysical Journal Supplement Series* **242** (2019) 2.
 - [119] M. P. van Daalen, J. Schaye, C. Booth and C. Dalla Vecchia, *The effects of galaxy formation on the matter power spectrum: a challenge for precision cosmology*, *Monthly Notices of the Royal Astronomical Society* **415** (2011) 3649–3665.
 - [120] I. G. McCarthy, J. Schaye, S. Bird and A. M. C. Le Brun, *The bahamas project: calibrated hydrodynamical simulations for large-scale structure cosmology*, *Monthly Notices of the Royal Astronomical Society* (2016) stw2792.
 - [121] N. E. Chisari, A. J. Mead, S. Joudaki, P. Ferreira, A. Schneider, J. Mohr et al., *Modelling baryonic feedback for survey cosmology*, *arXiv preprint arXiv:1905.06082* (2019) .
 - [122] A. Schneider, R. Teyssier, J. Stadel, N. E. Chisari, A. M. Le Brun, A. Amara et al., *Quantifying baryon effects on the matter power spectrum and the weak lensing shear correlation*, *Journal of Cosmology and Astroparticle Physics* **2019** (2019) 020.

- [123] E. Ayçoberry, V. Ajani, A. Guinot, M. Kilbinger, V. Pettorino, S. Farrens et al., *Unions: The impact of systematic errors on weak-lensing peak counts*, 2022. 10.48550/ARXIV.2204.06280.
- [124] K. Osato, M. Shirasaki and N. Yoshida, *IMPACT OF BARYONIC PROCESSES ON WEAK-LENSING COSMOLOGY: POWER SPECTRUM, NONLOCAL STATISTICS, AND PARAMETER BIAS*, *The Astrophysical Journal* **806** (jun, 2015) 186.
- [125] A. J. Mead, J. A. Peacock, C. Heymans, S. Joudaki and A. F. Heavens, *An accurate halo model for fitting non-linear cosmological power spectra and baryonic feedback models*, *Monthly Notices of the Royal Astronomical Society* **454** (2015) 1958–1975.
- [126] T. Tröster, C. Ferguson, J. Harnois-Déraps and I. G. McCarthy, *Painting with baryons: augmenting n-body simulations with gas using deep generative models*, *Monthly Notices of the Royal Astronomical Society: Letters* **487** (2019) L24–L29.
- [127] A. Schneider and R. Teyssier, *A new method to quantify the effects of baryons on the matter power spectrum*, *Journal of Cosmology and Astroparticle Physics* **2015** (2015) 049.
- [128] A. Schneider, S. K. Giri, S. Amodeo and A. Refregier, *Constraining baryonic feedback and cosmology with weak-lensing, x-ray, and kinematic sunyaev-zeldovich observations*, *arXiv preprint arXiv:2110.02228* (2021) .
- [129] M. Raveri and W. Hu, *Concordance and discordance in cosmology*, *Physical Review D* **99** (2019) 043506.
- [130] M. Raveri, G. Zacharegkas and W. Hu, *Quantifying concordance of correlated cosmological data sets*, *Physical Review D* **101** (2020) 103527.
- [131] M. Raveri and C. Doux, *Non-gaussian estimates of tensions in cosmological parameters*, *Physical Review D* **104** (2021) 043504.
- [132] Peel, Austin, Pettorino, Valeria, Giocoli, Carlo, Starck, Jean-Luc and Baldi, Marco, *Breaking degeneracies in modified gravity with higher (than 2nd) order weak-lensing statistics*, *A&A* **619** (2018) A38.
- [133] J. Liu, A. Petri, Z. Haiman, L. Hui, J. M. Kratochvil and M. May, *Cosmology constraints from the weak lensing peak counts and the power spectrum in cfhtlens data*, *Physical Review D* **91** (2015) 063507.
- [134] A. Petri, M. May, Z. Haiman and J. M. Kratochvil, *Impact of spurious shear on cosmological parameter estimates from weak lensing observables*, *Physical Review D* **90** (2014) 123015.
- [135] T. Eifler, P. Schneider and J. Hartlap, *Dependence of cosmic shear covariances on cosmology-impact on parameter estimation*, *Astronomy & Astrophysics* **502** (2009) 721–731.
- [136] C. B. Morrison and M. D. Schneider, *On estimating cosmology-dependent covariance matrices*, *Journal of Cosmology and Astroparticle Physics* **2013** (2013) 009.
- [137] J. A. Blazek, N. MacCrann, M. Troxel and X. Fang, *Beyond linear galaxy alignments*, *Physical Review D* **100** (2019) 103506.
- [138] S. v. d. Walt, S. C. Colbert and G. Varoquaux, *The numpy array: a structure for efficient numerical computation*, *Computing in Science & Engineering* **13** (2011) 22–30.
- [139] P. Virtanen, R. Gommers, T. E. Oliphant, M. Haberland, T. Reddy, D. Cournapeau et al., *Scipy 1.0: fundamental algorithms for scientific computing in python*, *Nature methods* **17** (2020) 261–272.
- [140] J. D. Hunter, *Matplotlib: A 2d graphics environment*, *Computing in science & engineering* **9** (2007) 90–95.
- [141] A. Lewis, *Getdist: a python package for analysing monte carlo samples*, *arXiv preprint arXiv:1910.13970* (2019) .